Textural evolution and trace element chemistry of hydrothermal calcites from Archean gold deposits in the Hattu schist belt, eastern Finland: Indicators of the ore-forming environment

Henrik Kalliomäki[a,*], Thomas Wagner[b], Tobias Fusswinkel[b], Dina Schultze[a]

[a] *University of Helsinki, Department of Geosciences and Geography, PO Box 64, University of Helsinki, Helsinki FI-00014, Finland*
[b] *Institute of Applied Mineralogy and Economic Geology, RWTH Aachen University, Wüllnerstr. 2, D-52062 Aachen, Germany*

ARTICLE INFO

ABSTRACT

Orogenic style gold mineralizations in the Archean Hattu schist belt (E Finland) are present in all major host rock lithologies including epiclastic sedimentary rocks, volcanic rocks, and felsic intrusives. The gold deposits are related to extensive quartz-dominated vein networks and the gold mineralization occurs as dissemination in altered wall rocks and within hydrothermal quartz veins. The quartz-dominated veins frequently contain calcite, which is also present within the country rocks. We analyze and compare the major and trace element chemistry of these calcites and test whether they carry the signatures of the origin of hydrothermal fluids associated with the gold deposits or record fluid interaction with the local wall rocks. The calcites show textural growth and chemical zoning, considerable chemical variations within samples and the chemical data do show some overlap between the samples. All calcites contain dominantly Ca with other elements being typically below 2 wt%, and they are accordingly classified as rather pure calcites. Amongst minor elements, both Mg and Fe show larger variations than Mn. The concentrations of most trace elements analyzed are relatively low, except for Sr and Y, which can attain values up to 1 wt% and 200 ppm, respectively. Some of the trace elements or trace element ratios in hydrothermal calcite, including Sr, Y, Mn, $(La/Lu)_N$ and ΣREE, show correlations with the respective host rock lithologies. This indicates that interaction between hydrothermal fluids and adjacent and diverse host rocks has strongly affected the trace element chemistry of calcite. Chemically variable growth zones in large calcite crystals and distinct grain populations within individual samples cannot be readily explained by host rock control, but instead they are interpreted to reflect changes in fluid composition over time. The hydrothermal calcites have chondrite-normalized REE patterns that are mostly HREE enriched relative to LREE, with very few exceptions that show unfractionated flat or LREE enriched (relative to the HREE) patterns. The REE patterns of the calcites are very different from those of their immediate host rocks, suggesting that they are inherited from the hydrothermal fluid(s) from which they precipitated. The HREE enrichment relative to the LREE visible in the patterns resembles the REE patterns of calcites from hydrothermal vein type deposits of metamorphic origin elsewhere and contrasts with the REE patterns of calcites from magmatic-hydrothermal environments. The REE patterns of the hydrothermal calcites in the Hattu schist belt deposits would therefore be compatible with formation from a fluid system that is essentially derived from metamorphic sources, in agreement with conclusions drawn from the fluid inclusion chemistry.

1. Introduction

Gold is produced from a diverse range of hydrothermal ore deposits, but approximately one third of the known global reserves classify as orogenic gold deposits and are typically hosted by regional metamorphic terranes including Archean greenstone belts and Phanerozoic schist belts (e.g. Goldfarb et al., 2001; Groves et al., 2003; Frimmel,

2008; Goldfarb and Groves, 2015). Typical features of most orogenic gold deposits are a syn- to late-timing of the mineralization relative to the peak metamorphism, location in fore- or back-arc settings, formation in broad thermal equilibrium with the country rocks (as indicated by the hydrothermal alteration assemblages), hydrothermal enrichment of K, S, CO_2, H_2O, Si and Au (with variable additions of As, B, Bi, Na, Sb, Te, and W), low base-metal contents, and gold precipitation from

medium- to low-salinity fluids which belong to the chemical system $H_2O–CO_2–NaCl–CH_4–N_2–H_2S$ (Gebre-Mariam et al., 1995; Mikucki, 1998; Groves et al., 1998; Ridley and Diamond, 2000; Goldfarb et al., 2001, 2005). The ultimate origin of the gold mineralizing fluids is still debated, and current models are favoring either a single source of fluids derived from devolatilization of metamorphic country rocks (Pettke et al., 2000; Phillips and Powell, 2010; Yardley and Cleverley, 2013; Goldfarb and Groves, 2015; Fusswinkel et al., 2017) or mixed sources with contributions from metamorphic fluids and fluids released from syntectonic felsic intrusions (Wang et al., 1993; Krienitz et al., 2008; Zoheir and Moritz, 2014; Molnár et al., 2016a).

Orogenic gold deposits are structurally controlled and typically hosted by second- and third-order structures where they form quartz dominated hydrothermal vein systems that carry native gold, sulfides (pyrite, pyrrhotite, arsenopyrite and chalcopyrite), carbonates (calcite, ankerite and siderite), tourmalines and tellurides as minor mineral phases (e.g. Groves et al., 1998; Mikucki, 1998). The chemical and isotopic composition of tourmaline has been commonly utilized as a petrogenetic proxy for the ore-forming environment and sources of gold mineralizing fluids (e.g. Krienitz et al., 2008; Hazarika et al., 2015; Molnár et al., 2016a; Kalliomäki et al., 2017), whereas the compositions of hydrothermal carbonates such as calcite have been used to a lesser extent (Kontak and Jackson, 1999; Sarangi et al., 2013; Dubinina et al., 2014; Hazarika et al., 2016). Despite the much simpler crystal-chemical structure compared to many silicate minerals, calcite can incorporate a wide range of trace elements (e.g. Veizer, 1983; Rimstidt et al., 1998 and references therein). Based on quantitative field and experimental studies, the geochemical characteristics of hydrothermal calcites, particularly the trace element and rare earth element (REE) composition, mainly reflect the chemistry of the fluids they have precipitated from (e.g. Terakado and Mazuda, 1988; Bau, 1991; Bau and Möller, 1992; Zhong and Mucci, 1995; Wogelius et al. 1997; Barker and Cox, 2011). In addition, there is a lattice-strain control on the incorporation of certain trace elements, which for example leads to preferential enrichment of divalent cations which form calcite-type mineral structures (e.g. Mg, Fe, Mn, Zn, and Co) and affects the fractionation of the rare earth elements (Rimstidt et al., 1998; Perry and Gysi, 2018 and references therein). Therefore, calcites from hydrothermal ore environments offer considerable potential for constraining key features of the mineralizing fluids and assessing the effects of fluid-rock interaction during fluid flow. Good examples where calcite chemistry has contributed to characterizing the ore-forming environment are studies of post-orogenic Pb-Zn veins in the Harz district in Germany (Möller et al., 1979, 1984), hydrothermal Mn-Fe-As veins in Permian rhyolites in southern Germany (Fusswinkel et al., 2013), Phanerozoic metasediment-hosted orogenic gold deposits of the Meguma terrane in Canada (Kontak and Jackson, 1999), the hydrothermal-metamorphic type Sukhoi Log Au deposit hosted by terrigenous-carbonate metasedimentary rocks in Russia (Dubinina et al., 2014) and Archean greenstone-hosted orogenic gold deposits in India (Sarangi et al., 2013; Hazarika et al., 2016).

The Archean Hattu schist belt (HSB), located in the Ilomantsi Greenstone belt in eastern Finland, hosts several orogenic style gold deposits. The formation of these deposits has been explained by alternative models involving 1) metamorphic fluids derived from large-scale devolatilization (Nurmi et al. 1993; Fusswinkel et al., 2017) or 2) contributions of metamorphic fluids and fluids released from felsic intrusives which are interpreted as coeval with the gold deposits (Molnár et al., 2016a). A regional scale study which tested the suitability of the trace element chemistry of hydrothermal tourmaline as a proxy for fluid sources in the HSB revealed a strong compositional signature from interaction of the hydrothermal ore-forming fluids with the diverse host lithologies (Kalliomäki et al., 2017). The orogenic gold deposits in the HSB are characterized by extensive quartz-dominated vein networks composed of multiple generations of veins. These veins contain hydrothermal calcites which occur also as a minor mineral phase in different host rocks of the ore deposits, including metavolcanics, metasedimentary rocks and felsic intrusives. In this paper, we report the results of a geochemical study of hydrothermal calcites from the Pampalo and Korvilansuo deposits of the HSB as well as the Kuittila tonalite suite. We characterize the major and trace element chemistry of calcites from hydrothermal veins and compare them with the data for disseminated calcites from the host rocks of the gold deposits (metavolcanics and felsic dikes). We further compare the geochemistry of hydrothermal calcites with calcite from the regional gold-mineralized Kuittila tonalite intrusion which could have contributed magmatic-hydrothermal fluids to the gold mineralizing system. The data make it possible to evaluate whether calcite geochemistry carries a clear signal of the hydrothermal fluids related to the ore forming environments and the fluid sources. They do also permit to directly link the calcite trace element chemistry with the composition of the ore-stage and late-stage hydrothermal fluids as determined from fluid inclusion studies (Fusswinkel et al., 2017).

2. Geological setting

2.1. The Hattu schist belt

The N-S striking Hattu schist belt, located in eastern Finland, comprises the easternmost supracrustal and intrusive suites of the Archean Ilomantsi greenstone belt and is located adjacent to, and extends across the border between Finland and Russia (Fig. 1). The Ilomantsi greenstone belt represents the youngest (ca. 2750 Ma; Huhma et al., 2012) of several Archean greenstone belts in the Karelian province and makes up the southwestern part of the Fennoscandian Archean craton. The Ilomantsi greenstone belt, and particularly the HSB, has been increasingly in the focus of research and exploration activity due to many occurrences of structurally controlled orogenic gold mineralization in the area (Fig. 1).

The HSB is predominantly composed of feldspathic epiclastic, volcanic and volcanoclastic rocks that are mostly intermediate and felsic in composition (Fig. 1). Smaller occurrences of ultramafic to mafic metavolcanics and banded iron formations are present in the HSB as well (Fig. 1). The geochronological U-Pb zircon ages for the Sivakkojoki Formation (2754 ± 6 Ma; Vaasjoki et al., 1993; Huhma et al., 2012) at the base and the Tiittalanvaara Formation (2726 ± 15 Ma; Vaasjoki et al., 1993) higher up in the succession demonstrate a rather short time interval for the deposition of the thick volcano-sedimentary package of the HSB. The sedimentary features have been interpreted in terms of a predominantly proximal turbiditic depositional environment, although the lowermost units may have formed at the transition between an earlier distal to a proximal environment (Sorjonen-Ward and Luukkonen, 2005). The Tiittalanvaara formation is overlain by the Pampalo formation, which was deposited in a transgressive or subsiding submarine setting with short-lived but diverse coeval volcanism (Sorjonen-Ward, 1993). The supracrustal sequences of the HSB are intruded by several series of intermediate to felsic plutonic rocks (granodiorites, tonalities and leucogranites) (Fig. 1). The intrusive nature of these granitoidic suites is evident from their field relations with the supracrustal units and also from the geochronological data (U-Pb ages of 2754 ± 4 to 2725 ± 6 Ma), which suggest syn- to post-tectonic emplacement (Sorjonen-Ward, 1993; Vaasjoki et al., 1993; Käpyaho et al., 2017). The depositional basement of the HSB is unknown, but an inherited ca. 3.0 Ga old zircon population that represents distinctly older crustal material is found within both supracrustal and plutonic rocks (Sorjonen-Ward and Claoué-Long, 1993; Vaasjoki et al., 1993; Heilimo et al., 2011; Huhma et al., 2012).

The present-day architecture of the HSB is characterized by transpressional N-NE trending dextral shear systems where granitoid plutons have been emplaced into dilatant sites, and where several individual shear zones are distinguishable (Sorjonen-Ward and Luukkonen, 2005). Progressive deformation has resulted in a regional geometry which is
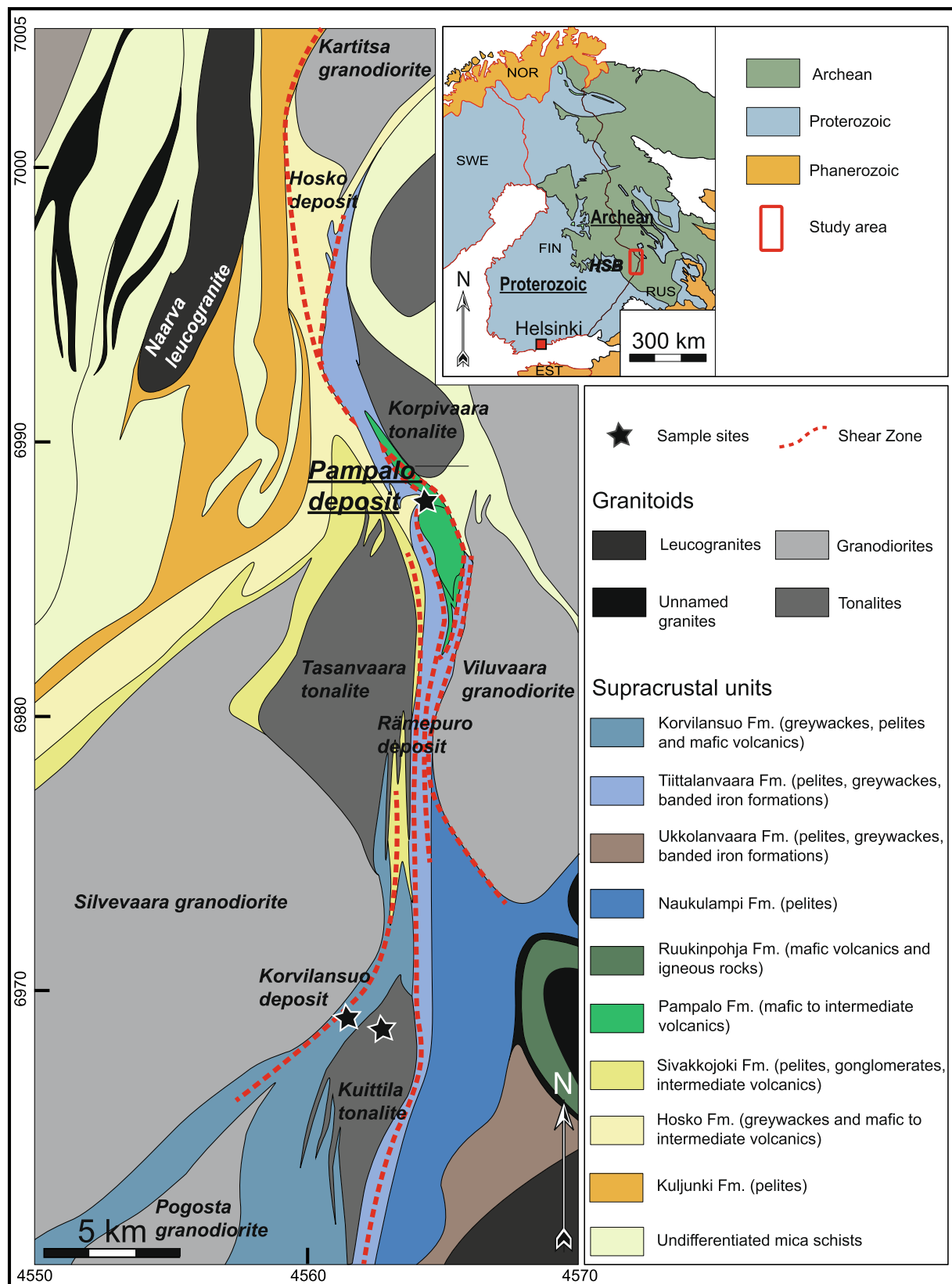
Fig. 1. Geological map of the Hattu schist belt (HSB), illustrating the main supracrustal units and granitoid intrusives, the major shear zones, orogenic gold deposits and sample sites. Redrawn and modified after Sorjonen-Ward (1993) and Sorjonen-Ward and Luukkonen (2005).

defined by upward-facing, generally steeply dipping structures (e.g. Sorjonen-Ward, 1993). Deformation, metamorphism and magmatism are closely related, and large-scale fluid flow focused into shear zones

has resulted in significant hydrothermal alteration of country rocks. Hydrothermally altered mineral assemblages in the HSB record Archean deformation and metamorphic overprint at greenschist to amphibolite

facies conditions (Kojonen et al., 1993) peaking at 480–590 °C and 3.4–6.0 kbar (O'Brien et al., 1993; Hölttä et al., 2012, 2016). Based on the results of recent pseudosection modeling and monazite geochronology, Hölttä et al. (2016) suggest a peak metamorphic event at 2660–2640 Ma which may have reached conditions as high as 570–670 °C and 6–7 kbar in the NE parts of the HSB. Finally, metamorphic overprint by the Paleoproterozoic Svecofennian orogeny (at ca. 1840 Ma; Hölttä et al., 2016) is manifested, in places, by greenschist facies mineral assemblages (Sorjonen-Ward, 1993).

2.2. Orogenic gold deposits in the Hattu schist belt

The gold deposits of the HSB share many common features, including host rock lithologies, structural setting, mineralization style and hydrothermal alteration, with other Archean orogenic gold provinces worldwide. Economically important gold mineralization has been identified in almost all rock types of the HSB, including metasedimentary rocks, mostly greywackes (the Korvilansuo, Rämepuro, and Hosko deposits), mafic to intermediate metavolcanics (the Pampalo deposit), tonalite intrusions (the Kuittila deposit), and felsic porphyry dikes associated with the metasedimentary and metavolcanic host rocks (Nurmi et al., 1993) (Fig. 1). Fluid flow and location of gold ore mineralization were controlled by the rheological and chemical contrast between adjacent lithological units (Sorjonen-Ward et al., 2015). Three major ore mineralization styles are recognized in the HSB, which are 1) an early Mo-W-(Au) stockwork mineralization related to the Kuittila tonalite, 2) the subsequent main orogenic-style Au-sulfide-telluride mineralization occurring primarily in quartz veins, and 3) the youngest disseminated Au-sulfide-telluride mineralization within host rocks (Kojonen et al., 1993; Molnár et al., 2016a).

Most of the gold ores in the HSB occur as dissemination within the strongly sheared supracrustal rocks, but especially in the Kuittila and Pampalo deposits, Au is also present within quartz ± tourmaline ± calcite veins. Pyrite and pyrrhotite are the principal sulfides associated with native gold, whereas chalcopyrite and arsenopyrite occur only in minor amounts (Kojonen et al., 1993). The Hosko deposit in the northern part of the HSB differs from the other deposits by carrying abundant arsenopyrite in the ore mineral assemblage. The Hosko deposit shows also other distinct features, such as a rather unusual chemical composition of tourmalines associated with gold mineralization (Molnár et al., 2016a; Kalliomäki et al., 2017) and hydrothermal alteration that pre-dates the regional foliation (Sorjonen-Ward et al., 2015). The gold-mineralizing processes in the HSB are associated with pervasive hydrothermal alteration resulting in potassic alteration, silicification, tourmalinization and carbonation of the wall rocks (Kojonen et al., 1993).

The relative time relationships between gold mineralization and peak metamorphism in the HSB are not yet fully established. The maximum age limit of gold introduction is defined by the 2745 ± 10 Ma U-Pb age of the mineralized Kuittila tonalite while the younger limit is interpreted as 2700 Ma (Vaasjoki et al., 1993). Based on the peak metamorphic growth of garnet porphyroblasts and dynamic recrystallization of gold bearing hydrothermal veins that overprint the gold mineralizations and associated hydrothermal alterations in the area, Sorjonen-Ward et al. (2015) infer that the metamorphic peak post-dates the mineralizations. However, they note that in the Pampalo deposit the time relations remain poorly constrained. The youngest constraint on Au mineralizations in the Pampalo deposit is given by the U-Pb age of hydrothermal zircon of 2710 Ma which is correlated with the onset of peak metamorphic, crustal reworking and magmatism in the area (Käpyaho et al., 2017). The Paleoproterozoic Svecofennian orogeny at ca. 1851–1795 Ma (Kontinen et al., 1992; Hölttä et al., 2016) has disturbed the isotopic signatures of hydrothermal minerals, has caused partial remobilization of gold in the deposits and may have led to entrapment of younger generations of fluid inclusions unrelated to the Archean hydrothermal gold mineralizing system (Poutiainen and

Partamies, 2003; Molnár et al., 2016b). The Paleoproterozoic remobilization was clearly highly localized, because unmodified and structurally early Archean gold ore veins with primary Au-rich (200–600 ppb of Au) fluid inclusions have been recorded in boudinaged felsic dikes of the Pampalo deposit. These veins are crosscut by younger sets of barren hydrothermal veins, which carry exclusively low-Au fluid inclusions which are still structurally related to the Archean deformational framework (Fusswinkel et al., 2017).

2.2.1. The Pampalo gold deposit

The stratigraphy of the Pampalo formation is well established due to excellent exposures in active open pit and underground mines. The Pampalo formation is the only lithological unit of the HSB that is dominated by metavolcanic rocks and contains the following units from base to top (see full description in Sorjonen-Ward, 1993; Sorjonen-Ward et al., 2015): 1) banded iron formations (BIF), 2) Mafic metavolcanics or metabasalts (MB) (as known in the older literature and in the reports of the local mining company) and dolerites, 3) intermediate volcaniclastic rock or andesitic tuffs (AT) (as known in the older literature and in the reports of the local mining company) which are intruded by felsic porphyry dikes (FP) along the shear zone, 4) ultramafic metavolcanics (UM), which are altered to talc-chlorite-carbonate schist in the eastern parts of the deposit, with intercalated felsic units and felsic porphyry dikes (Fig. 2). The Pampalo gold deposit is hosted by one of the major shear zones in the HSB (Figs. 1 and 2) and the main economic gold mineralization is present as dissemination in the altered andesitic tuffs and felsic porphyry dikes and as sets of quartz + K-feldspar + pyrite veins. Both the andesitic tuffs and the felsic porphyry dikes show extensive quartz + K-feldspar + biotite + sericite + carbonate alteration. The adjacent metabasalts host intense quartz + calcite + tourmaline + pyrite veining and show distal-style carbonate + sulfide alteration.

Based on field relationships and the ore and gangue mineral assemblages, three major hydrothermal vein generations have been recognized in the Pampalo deposit (Fusswinkel et al., 2017): 1) early quartz + K-feldspar + calcite + pyrite ± gold veins, 2) younger quartz + calcite + tourmaline + pyrite veins, and 3) late quartz ± fluorite ± galena ± sphalerite veins. The early generation of quartz + K-feldspar + calcite + pyrite ± gold veins is present as sets of veins trending NE along the main foliation in the andesitic tuff and felsic porphyry dikes, and less frequently in the metabasalts. The felsic porphyry dikes are strongly silicified and highly mineralized, have the highest Au grades in the deposit and show abundant boudinage. Commonly, the boudin necks of the felsic porphyry dikes contain an infill mineralization which is identical to that of the early vein generation. The two younger vein generations crosscut the main pervasive foliation as well as the early vein type. Vein generation 2) is present as tension gashes and vein generation 3) are extension veins which in turn crosscut the veins of generation 2). Locally, a very late crosscutting generation of hydrothermal veins representing a fourth type is present, which contains quartz, calcite, muscovite and gypsum. All the fluid types, despite characteristics differences, related to the major vein generations shows the signature of orogenic gold fluids, i.e. low- to intermediate-salinity, presence of CO_2, CH_4 or N_2, high S contents, enrichment in B, As, Sb and W, and low Pb and Zn concentrations (Fusswinkel et al., 2017).

3. Samples and methods

3.1. Sampling

The sampling targeted calcite bearing hydrothermal veins and host rocks of the Pampalo and Pampalo East Au deposits, covering all major lithologies including metavolcanics and felsic porphyry dikes. Representative samples were collected from the Pampalo underground mine and supplemented with samples from selected drill cores. For
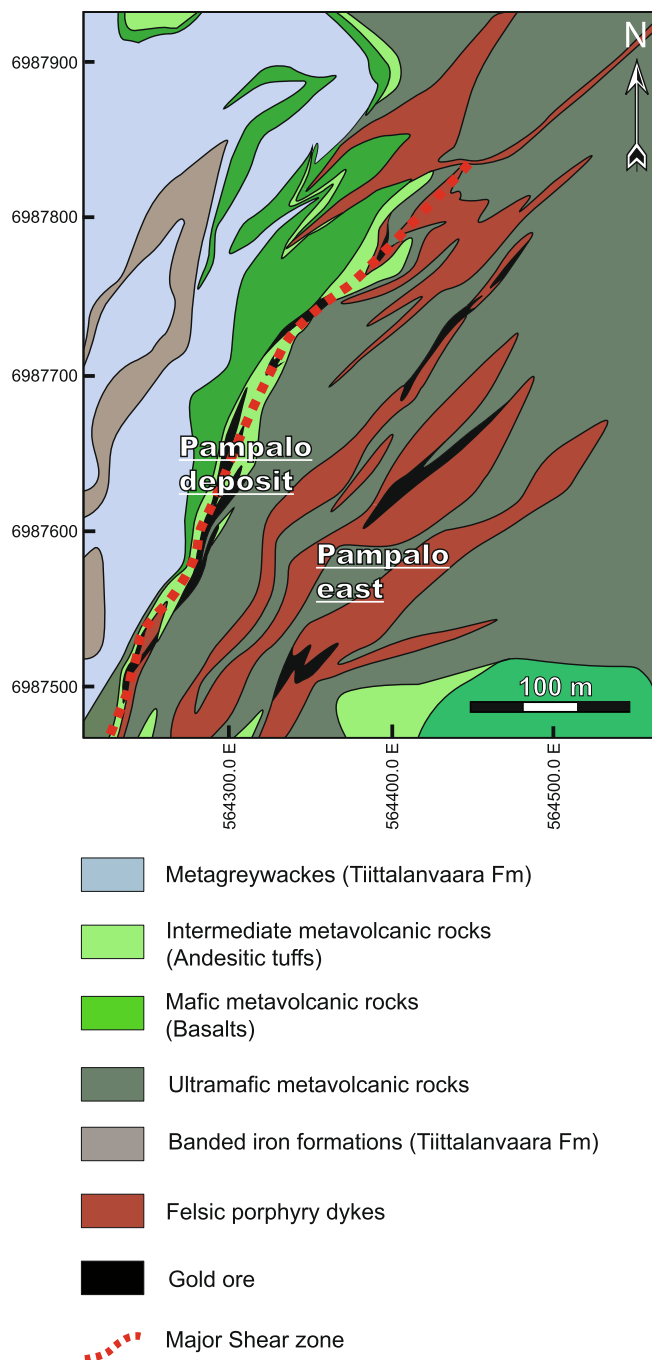
Fig. 2. Local geology of the Pampalo and Pampalo East orogenic gold deposits. Redrawn and modified after Parkkinen (1994).

comparison, calcite bearing samples from the Korvilansuo Au deposit, hosted by metasedimentary and felsic porphyry dikes, and from the Kuittila tonalite were sampled as well. A detailed list of the samples along with a short description is given in Table 1. A subset of the hydrothermal vein samples used in this study were already used in the fluid inclusion study of Fusswinkel et al. (2017). The major element composition of carbonates was analyzed from a total number of 18 samples, and trace element and REE analysis was performed on 17 of these. All analyzed samples were also petrographically studied by conventional transmitted-light microscopy and optical cathodoluminescence (CL) imaging to detect possible growth zoning.

3.2. Electron probe microanalysis (EPMA)

The major element composition of calcites was determined by wavelength-dispersive electron probe microanalysis with the JEOL JXA-8600 Superprobe instrument, upgraded with SAMx hardware and the XMAs/IDFix/Diss5 analytical and imaging software package, at the Department of Geosciences and Geography, University of Helsinki. The quantitative wavelength-dispersive spectrometry (WDS) measurements were performed with focused beam, 15 kV acceleration voltage and 10nA beam current. Details about the analytical configuration used are summarized in Table 2. The limits of detection for the analyzed elements are: 0.06 wt% (Na, Mg), 0.07 wt% (Ca, Mn), 0.09 wt% (Fe, Ni), 0.15 wt% (Sr) and 0.26 wt% (Ba).

3.3. Optical cathodoluminescence imaging

Cathodoluminescence microscopy of calcite bearing thick sections was performed with a Cambridge Image Technology Limited (CITL) CL8200 Mk5-2 optical cold cathodoluminescence stage mounted onto a Leica DM2700P polarization microscope equipped with a Peltier-cooled DFC-450C high-resolution digital camera. CL imaging of carbonates was done with an acceleration voltage of 7.5 kV and a beam current of 250 μm.

3.4. Laser ablation-inductively coupled plasma-mass spectrometry (LA-ICP-MS)

The trace element and REE concentrations in calcites have been analyzed with the LA-ICP-MS system at the Department of Geosciences and Geography at the University of Helsinki. This system couples a Coherent GeoLas MV 193 nm excimer laser ablation system to an Agilent 7900 s quadrupole ICP mass spectrometer. Spot sizes between 60 and 90 μm were used for LA-ICP-MS analysis of calcite, depending on the grain size. The laser repetition rate was set to 10 Hz. The flow rates of Ar plasma gas, He carrier gas and Ar auxiliary gas were set to 15 L/min, 1.0 L/min and 0.85 L/min, respectively. The analytical conditions are listed in Table 3. The reference material NIST SRM 610 was used to bracket sample analysis and as external standard. As an internal standard, the Ca values determined by EPMA were used. Accuracy of the analysis was tested daily by replicate analysis of NIST SRM 612 as an unknown sample, and the long-term accuracy was better than 5% for most elements. The SILLS software package (Guillong et al., 2008) was used for data reduction following procedures outlined in Heinrich et al. (2003). Data analysis with SILLS made it possible to detect inclusions of other minerals in calcite in the time-resolved LA-ICP-MS signals. The inclusions are clearly distinguishable in the LA-ICP-MS signals by a simultaneous sharp increase in the count rate of the elements present in such mineral inclusions. The presence of micro-inclusions, especially of fluid inclusions manifested by a sudden increase in Na count rates, was quite commonly observed in the calcite signals. Segments of the LA-ICP-MS signals affected by mineral or fluid inclusions were excluded from the integration window used for calculation of element concentrations in calcite. In cases of too short signals or signals with multiple inclusions being present, the elements affected by micro-inclusions were excluded from the dataset.

4. Results

4.1. Calcite occurrences and petrographic relationships

Calcites are a common mineral phase in the hydrothermal veins within the HSB, but they do also occur as disseminations within supracrustal rocks and intrusives (including felsic porphyry dykes and tonalite intrusions). In the hydrothermal veins, calcite is a common mineral phase and the veins are found in all major rock lithologies in the HSB gold deposits (Fig. 3A to 3G). Disseminated calcite is less

Table 1

Sample list of different calcites from the Hattu schist belt with their locality, host rock and coexisting mineral phases and sulfides. In bold are marked samples correlated to the vein generations of Fusswinkel et al. (2017) which are marked as (1) early generation veins and (2) younger tension gash veins and (3) late extensional veins. The calcite in the sample PAM-10 may represent either vein or quartz + calcite rich layer within the metavolcanic host rocks. Mineral abbrevations are: Calc = calcite, Qt = quartz, K-fed = K-feldspar, Tur = tourmaline, Epi = epidote, Bt = biotite, Mus = muscovite, Chl = chlorite, Tlc = talc, Amp = amphibole, Py = pyrite, Po = pyrrhotite, Ccp = chalcopyrite, Gn = galena, Acc = accessorial. Hostrock abbrevations are: FP = felsic porphyry, AT = andesitic tuff (intermediate volcanic rock), MB = metabasalt (mafic volcanic rock), UM = ultramafic volcanic rock, MS = mica schist (presumably metagreywackes), Ton = tonalite.

Sample	Type	Locality	Host rock	Mineralogy	Sulfides	Relation to main ore zones
PAM-7 (3)	Vein	Pampalo	Unknown	Qt, Calc, K-fed	Py, Gn	Unknown
PAM-18 (1)	Vein	Pampalo	FP	Calc, K-fed, Qt, Ms,	Py (Po in crags of Py grains)	Ore zone
PAM-3a (1)	Vein	Pampalo	AT	Calc, K-fed, Qt (acc:Bt)	Py (only few grains)	Ore zone
PAM-80.55 (1)	Vein	Pampalo	FP	Qt, Calc, K-fed,	Py (only few grains)	Ore zone
PAM-5 (2 or 3)	Vein	Pampalo	FP	K-fed, Calc, Tur (acc:Qt)	Po	Ore zone
PAM-5	Host rock	Pampalo	FP	K-fed, Calc, Tur (acc:Qt)	Po	Ore zone
PAM-15 (1)	Vein	Pampalo	FP	Qt, Calc, K-fed	Py	Ore zone
PAM-67.6 (2)	Vein	Pampalo	MB	Qt, K-fed, Calc, Bt, Tur (acc. Chl)	-	Barren
PAM-51.0	Vein	Pampalo	MB	Qt, Calc, Tur, Ep	Po, Ccp	Barren
PAM-51.5	vein	Pampalo	MB	Calc, Qt, Tur, Ep	Po, Ccp	Barren
PAM-10	n/a	Pampalo	AT	Bt, Qt, Calc	Py (only few grains)	Ore zone
PAM-31 (1)	Vein	Pampalo	FP	Calc (acc:Bt)	Po	Ore zone
PAM-9	Host rock	Pampalo	FP	Calc, Qt, Chl,	Py, Po (Po replacing Py)	Ore zone
PAE-12 (1)	Vein	Pampalo E	AT	Qt, Calc	Py	Unknown
PAE-9	Hostrock	Pampalo E	UM	Tlc, Tur, Amp, Calc, Qt	Py	Unknown
PAE-7	Vein	Pampalo E	UM	Calc, Qt, K-fed	Ccp (only few grains)	Unknown
PAE-7	Hostrock	Pampalo E	UM	Chl, Bt, Amp, Calc, Tur (acc:Tlc)	Py, Ccp	Unknown
MHS-12	Hostrock	Korvilansuo	FP	Qt, K-fed, Calc (acc:Tur, Epi, Chl)	Py, Po, Ccp	Ore zone
MHS-12	Vein	Korvilansuo	FP	Calc (acc:Qt)	Po	Ore zone
MHS-10b	Vein	Korvilansuo	MS	Calc, Qt	–	Ore zone
KUI-1	Host rock	Kuittila	TON	Qt, K-fed, Bt, Ms, Calc	–	Barren

Table 2

Configuration of wave length dispersive (WDS) for electron microprobe analysis.

Element	Standard	Line	Crystal
Na	Albite	Ka	TAP
Mg	Dolomite	Ka	TAP
Ca	Calcite	Ka	PET
Mn	Rhodonite	Ka	LIF
Fe	Haematite	Ka	LIF
Ni	NiSi	Ka	LIF
Sr	Celestite	La	TAP
Ba	Barite	La	PET

common in the metasedimentary rocks, metavolcanics and granitoids and often occurs as a minor phase (Table 1; Fig. 3.I). In the felsic porphyry dikes of the Pampalo (PAM-5) and Korvilansuo (MHS-12) deposits, some of the hydrothermal calcites show textures resembling those in the hydrothermal veins, but clear contacts to host rocks and crosscutting relationships to other veins are missing. These hydrothermal calcites have most probably formed when hydrothermal fluids infiltrated and altered the host rocks. Accordingly, these calcites are classified as host rock calcites instead of vein calcites.

Detailed descriptions of the mineralogical composition of the samples investigated are summarized in Table 1. Quartz is the main mineral

phase coexisting with calcite in the hydrothermal veins, together with K-feldspar and tourmaline (Fig. 3A, 3B, 3G and 3H). Where present, biotite and chlorite are the dominant sheet silicates associated with hydrothermal calcites (Fig. 3D). Essentially the same mineral phases are found in the felsic porphyry dikes (e.g. MHS-12) and the tonalite intrusive (KUI-1) where disseminated calcites are present. Calcites are also present within the ultramafic metavolcanics (PAE-9), which are otherwise mainly composed of amphibole, tourmaline and talc (Fig. 3I). Epidote is commonly present in those samples that show stronger alteration (e.g. PAM-51.0, PAM-51.5). As typical in the entire HSB, pyrite and pyrrhotite are the most common sulfides (Fig. 3F and 3E; Table 1), but in some of the late veins (e.g. PAM-7; Table 1) galena is also abundant (Fig. 3H). Pyrite is the dominant sulfide in most Pampalo samples (Fig. 3E), but pyrrhotite is present as well, and in places replaces pyrite (Fig. 3F). In contrast, pyrrhotite is the dominant sulfide in the samples from the Korvilansuo deposit. The calcites typically occur as euhedral or subhedral grains up to several mm or even cm in size within coarser-grained veins (Fig. 3). The grain size tends to be generally smaller for the calcites within the host rocks and their altered equivalents. The calcite crystals appear often relatively fresh, even when alteration (e.g. sericitization or saussuritization) of other minerals such as feldspars is evident.

Different successive stages of calcite growth are manifested by concentric growth zoning detected by cathodoluminescence imaging in

Table 3

Summary of instrumental parameters used for calcite LA-ICPMS analysis.

|	
Laser system	Coherent GeoLas Pro MV excimer
Wavelength	193 nm
Energy density for calcite ablation	7 J/cm^2
Repetition rate	10 Hz
Ablation spot size	60 μm, 90 μm (depending on the grain size)
Carrier gas flow (He)	1.0 l/min
ICP-MS	Agilent 7900 s
Plasma gas flow (Ar)	15 l/min
Auxiliary gas flow (He)	0.85 l/min
Measured isotopes	Na23, Mg24, Si29, P31, Ca44, Sc45, V51, Cr52, Mn55, Fe57, Co59, Ni60, Cu63, Zn66, Sr88, Y89, Ag107, Cd111, Sn118, Ba137, La139, Ce140, Pr141, Nd145, Sm147, Ey151, Gd157, Gd157, Tb159, Dy161, Ho165, Er166, Tm169, Yb172, Lu175, Au197, Pb208.
Dwell times	0.01 s, except all REE 0.02 s
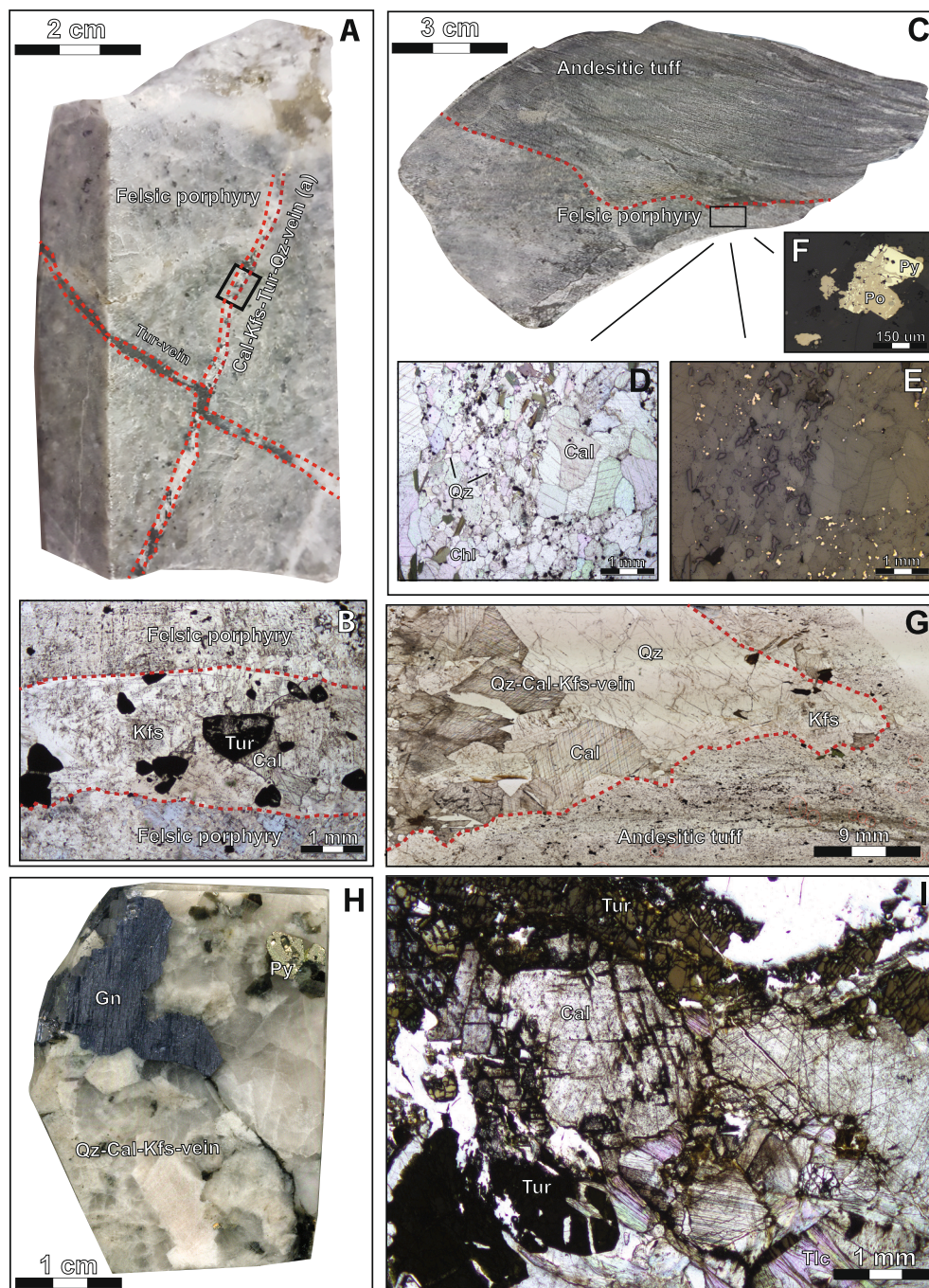
Fig. 3. Hand specimen photographs and photomicrographs illustrating the textural relationships of the different hydrothermal calcite types of the Hattu schist belt, eastern Finland. (A) Hand specimen photograph of calcite + K-feldspar + tourmaline (+ quartz) vein in felsic porphyry dike; Pampalo deposit (sample PAM-5). (B) Photomicrograph of calcite + K-feldspar + tourmaline (+ quartz) vein in felsic porphyry dike; Pampalo deposit (sample PAM-5). (C) Hand specimen photograph of calcite bearing felsic porphyry dike in contact to andesitic tuff; Pampalo deposit (sample PAM-9). (D) Transmitted-light photomicrograph of calcite bearing felsic porphyry dike containing chlorite, quartz and sulfides as minor minerals; Pampalo deposit (sample PAM-9). (E) Reflected-light photomicrograph of fine-grained sulfides in the calcite bearing felsic porphyry dike; Pampalo deposit (PAM-9). (F) Reflected-light photomicrograph of pyrite replaced by pyrrhotite in calcite bearing felsic porphyry dike; Pampalo deposit (sample PAM-9). (G) Photomicrograph illustrating contact between andesitic tuff and quartz + calcite + K-feldspar vein. Euhedral calcite crystals in the vein are representative of the coarser-grained calcites in the HSB samples; Pampalo deposit (sample PAM-3a). (H) Hand specimen photograph of late-stage quartz + calcite + K-feldspar vein with coarse-grained galena and pyrite; Pampalo deposit (sample PAM-7). (I) Photomicrograph of disseminated calcite in the ultramafic host rock composed mainly of talc, amphibole and tourmaline; Pampalo East deposit (PAE-9). Mineral abbreviations: Cal: calcite, Tur: tourmaline, Qz: quartz, Kfs: K-feldspar, Chl: chlorite, Tlc: talc, Gn: galena, Py: pyrite, Po: Pyrrhotite.

three samples (PAM-7, PAM-80.55 and PAM-51.0) (Fig. 4). These samples contain calcite crystals that show several growth zones distinguished by different luminescence intensities and sharp contacts between the individual zones (Fig. 4A to 4F). However, calcite grains lacking detectable zoning pattern are present in these samples as well (Fig. 4C and D). In addition to zoning, the sample PAM-51.0 contains two different populations of calcite grains with contrasting CL colors (Fig. 4G). BSE imaging revealed that the calcite grains with the brighter CL color contains large amounts of micro-inclusions that are not present in the calcite grains with the darker CL color (see Supplementary Fig. SF1). In places, the calcites show also irregular variations of the CL intensity that are different from a typical concentric growth zoning. Especially the areas close to grain boundaries and cracks may have different CL intensities, which could potentially be related to the local alteration by interaction with a hydrothermal fluid or differences in

physical topography of the grain. These small-scale textural features which document multiple stages of calcite growth are not recognizable by conventional optical microscopy, which highlights the importance of supporting micro-analytical studies by detailed CL imaging of the samples.

4.2. Major element chemistry

The average major element compositions of calcites are presented in Table 4 and the data are plotted into the Ca-Mn-(Mg + Fe) diagram in Fig. 5. The complete EPMA dataset is reported in the Electronic Supplementary Material (Table ST1). The average Mg, Fe and Mn concentrations of different calcites are in the range of 0.14–0.87 wt%, 0.22–1.15 wt% and 0.54–1.96 wt%, respectively, while the Ca concentrations vary between 50.6 and 55.2 wt%. Based on the major
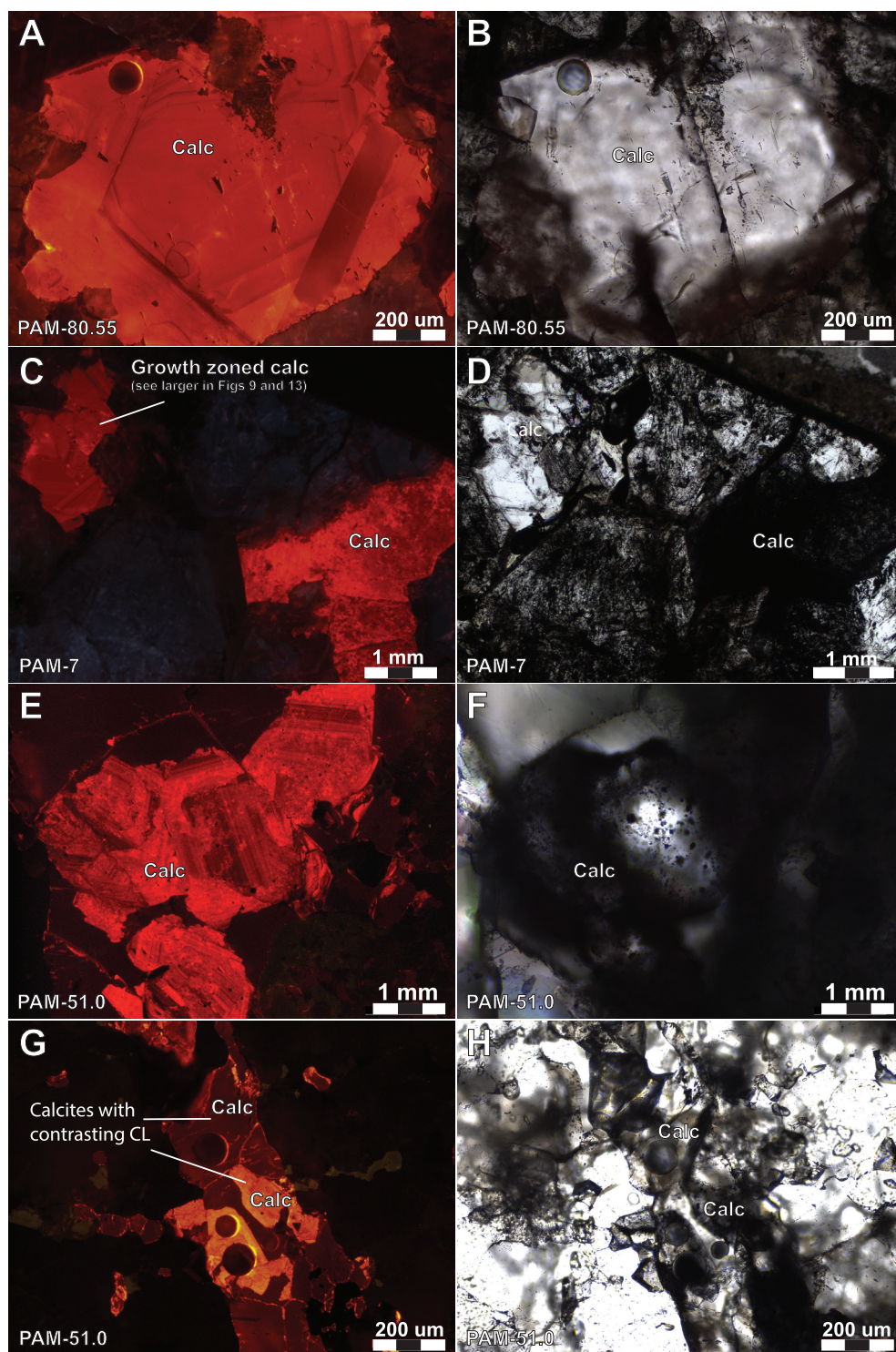
Fig. 4. Cathodoluminescence and corresponding transmitted-light images of hydrothermal calcites from the Pampalo deposit showing chemically distinct growth zoning (A-F) and grain populations (G and H). (A) and (B) are growth zoned calcites in a hydrothermal vein (PAM-80.55) hosted by felsic porphyry dike. (C) and (D) are growth zoned calcites (see larger images in Figs. 9 and 13) and unzoned calcites (right lower corner) in hydrothermal vein (PAM-7). (E) and (F) are growth zoned calcites in the hydrothermal vein (PAM-51.0) hosted by the mafic metavolcanics. (G) and (H) are two populations of calcite grains with distinct CL intensities in the hydrothermal vein (PAM-51.0) hosted by the mafic metavolcanics.

element composition, all the analyzed carbonate phases can be classified as rather pure calcites except two samples from the Pampalo East deposit (PAE-12 and PAE-7) where additionally Mg-calcite and dolomite phases were recognized (Table 4; Fig. 5). The Mg-calcites in the sample PAE-12 (only one analyzed grain) have Mg concentrations of 0.1 apfu, which places them at the boundary between calcite and Mg-calcite. The Mg-rich carbonates from sample PAE-7 typically have Mg concentrations of up to 0.4 apfu, which conforms to dolomite.

Although the concentrations of Mg, Fe and Mn in calcite are generally rather low, the calcites nevertheless show some variations in the Ca-Mn-Mg-Fe compositional spaces (Fig. 5). Especially, the

compositional variations within samples are distinguishable along the Ca-(Mg + Fe) binary (Fig. 5a), while the variations between the samples are better portrayed in the Mg-Fe-Mn diagram (Fig. 5c). Because the concentration of all elements other than Ca are typically at the level of minor elements (< 2.4 wt%), the concentrations of Mg, Fe and Mn were also analyzed with LA-ICP-MS. These results are reported in the Electronic Supplementary Material (Table ST1). The typical variations of the Mg, Fe and Mn concentrations within individual calcite samples are in the same range as variations between different samples, reaching at maximum one order of magnitude (Table 4; Table ST1 in Electronic Supplementary Material). We analyzed profiles through individual

Table 4

Representative average major elemental compositions (in wt.% and apfu) of calcites from the Hattu schist Belt. *CO_2 values are calculated. Abbrevatio-ns: u.d.l. = under the limit of detection, FP = felsic porphyry, AT = andesitic tuff (intermediate volcanic rock), MB = metabasalt (mafic volcanic rock), UM = ultramafic volcanic rock, MS = Mica schist (presuambly metagreywacke), Ton = tonalite.

Sample	PAM-18	PAM-80.55	PAM-15	PAM-7	PAM-5	PAM-5	PAM-31	PAM-9	MHS-12	MHS-12	MHS-10	KUI-1
Host rock	FP	FP	FP	FP	FP	FP	FP	FP	FP	FP	MS	TON
wt.%	Vein	Vein	Vein	Vein	Vein	Host rock	Vein	Vein	Host rock	Vein	Vein	Host rock
MgO	0.43	0.16	0.28	b.d.	0.36	0.33	b.d.	0.57	0.39	0.37	0.29	0.61
CaO	52.65	54.56	51.89	54.87	54.30	52.53	53.10	52.58	54.96	54.87	50.64	55.21
MnO	1.96	1.02	0.99	1.00	1.44	1.38	0.87	1.49	1.15	1.14	1.20	1.12
FeO	1.14	0.34	0.99	0.34	0.81	0.77	0.22	1.00	0.53	0.55	0.66	0.98
SrO	0.74	0.45	0.20	b.d.	b.d.	b.d.	b.d.	0.88	0.26	0.37	b.d.	0.27
BaO	b.d.	b.d.	b.d.	b.d.	b.d.	b.d.	b.d.	b.d.	b.d.	b.d.	b.d.	0.28
CO_2*	43.85	43.74	42.20	43.87	44.40	42.91	42.23	43.73	44.62	44.52	41.20	45.29
Total	100.44	99.85	96.31	100.04	101.31	97.92	96.21	100.08	101.72	101.52	93.98	103.23
Formula (O = 3)												
Mg	0.01	0.00	0.01		0.01	0.01		0.01	0.01	0.01	0.01	0.01
Ca	0.94	0.98	0.96	0.98	0.96	0.96	0.99	0.94	0.96	0.97	0.96	0.96
Mn	0.03	0.01	0.01	0.01	0.02	0.02	0.01	0.02	0.02	0.02	0.02	0.02
Fe	0.02	0.00	0.01	0.00	0.01	0.01	0.00	0.01	0.01	0.01	0.01	0.01
Sr	0.01	0.01	0.00						0.01	0.00	0.00	0.00
Ba												0.00
% Molecule												
$CaCO_3$	94.23	97.91	96.49	98.16	95.98	96.07	98.69	94.38	96.48	96.72	96.46	95.67
$MgCO_3$	1.06	0.30	0.73		0.89	0.84		1.42	0.94	0.91	0.76	1.46
$MnCO_3$	2.77	1.44	1.46	1.41	2.01	1.99	1.27	2.11	1.60	1.59	1.80	1.53
$FeCO_3$	1.59	0.48	1.44	0.47	1.12	1.10	0.32	1.39	0.73	0.75	0.98	1.32
$SrCO_3$	0.72	0.69	0.21					0.84	0.25	0.35		0.25
$BaCO_3$										0.00		0.18
Classification	Calcite	Calcite	Calcite	Calcite	Calcite	Calcite	Calcite	Calcite	Calcite	Calcite	Calcite	Calcite

Sample	PAM-3a	PAM-10	PAM-51.0	PAM-51.5	PAM-67.7	PAE-12	PAE-12	PAE-7	PAE-7	PAE-9
Host rock	AT	AT	MB	MB	MB	AT	AT	UM	UM	UM
wt.%	Vein	n/a	Vein	Vein	Vein	Vein	Vein	Host rock	Host rock	Host rock
MgO	0.29	0.37	0.50	0.14	0.57	3.79	0.87	17.10	0.70	0.65
CaO	52.68	53.63	54.04	54.20	53.10	44.71	50.90	30.78	54.10	53.36
MnO	1.32	0.92	0.57	0.72	0.66	0.98	0.77	0.83	0.54	0.66
FeO	0.61	0.87	1.15	0.66	0.97	2.42	0.79	5.75	0.63	0.85
SrO	1.41	0.56	b.d.	b.d.	b.d.	0.36	0.18	0.12	0.36	b.d.
BaO	b.d.	b.d.	b.d.	b.d.	b.d.	b.d.	b.d.	b.d.	0.30	b.d.
CO_2*	43.20	43.83	43.94	43.48	43.30	41.47	41.81	46.87	43.96	43.50
Total	99.00	100.18	100.09	99.15	98.61	93.72	95.14	101.35	99.97	99.01
Formula (O = 3)										
Mg	0.01	0.01	0.01	0.00	0.01	0.10	0.02	0.40	0.02	0.02
Ca	0.96	0.96	0.97	0.98	0.96	0.85	0.96	0.52	0.97	0.96
Mn	0.02	0.01	0.01	0.01	0.01	0.01	0.01	0.01	0.01	0.01
Fe	0.01	0.01	0.02	0.01	0.01	0.04	0.01	0.08	0.01	0.01
Sr	0.01	0.01				0.00	0.00	0.00	0.00	
Ba									0.00	
% Molecule										
$CaCO_3$	95.69	96.02	96.53	97.83	96.23	84.62	95.56	51.54	96.59	96.25
$MgCO_3$	0.72	0.92	1.24	0.35	1.45	9.97	2.25	39.84	1.74	1.62
$MnCO_3$	1.90	1.30	0.81	1.02	0.95	1.46	1.14	1.10	0.77	0.93
$FeCO_3$	0.86	1.22	1.61	0.93	1.37	3.58	1.15	7.51	0.88	1.19
$SrCO_3$	1.40	0.55					0.37	0.18	0.11	0.35
$BaCO_3$									0.20	
Classification	Calcite	Calcite	Calcite	Calcite	Calcite	Mg-calcite	Calcite	Dolomite	Calcite	Calcite

calcite crystals in samples PAM-3a, PAM-9 and PAM-51.5 where growth zoning was not detected by optical microscopy and CL imaging (Fig. 6A, 6C and 6E). These samples did not reveal any systematic chemical zoning, but some minor compositional changes across the grains is demonstrated by CaO concentrations varying by up to 3.6 wt% and MnO by about 1.0 wt% (Fig. 6B, D and F).

Vein calcites hosted by the felsic porphyry dikes in the Pampalo (PAM-5) and Korvilansuo (MHS-12) deposits show essentially Mg, Fe and Mn compositions which are comparable to those of the disseminated calcites in their respective host rocks. In the Korvilansuo deposit, the calcites related to the felsic porphyry dikes have also a composition which is similar to the vein calcites hosted by the mica schist (MHS-10). By contrast, the Mn concentrations in different calcites from the Pampalo and Pampalo East deposits (all samples with the codes PAM and PAE) appear to vary between different host rock lithologies. Calcites related to ultramafic and mafic rock types have considerably lower Mn concentrations (0.54–0.83 wt% MnO) than calcites related to andesitic tuff (0.77–1.32 wt% MnO) and felsic porphyry dikes (0.87–1.96 wt% MnO). The Mg-calcites and dolomites (samples PAE-7 and PAE-12) have average concentrations of 0.83 and 0.92 wt% MnO, which is slightly higher than the Mn concentrations in calcites from the same samples.

4.3. Trace element characteristics

The average trace element compositions (including the REE) of different calcite types are summarized in Table 5 and the compositional variations of selected elements are illustrated in Fig. 7. The complete dataset is reported in the Electronic Supplementary Material (Table ST2). The average concentrations of many elements analyzed are
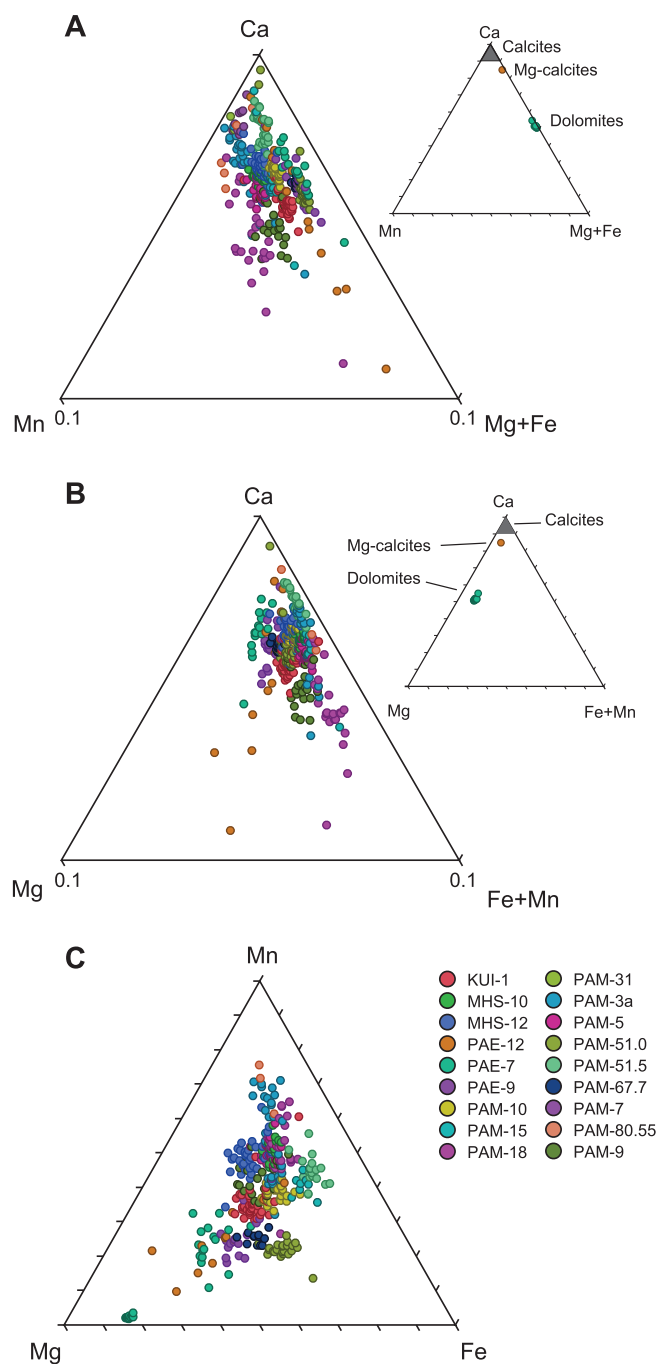
Fig. 5. Ternary diagrams illustrating the major element composition of hydrothermal calcites from the Hattu schist belt. (A) System Ca-Mn-(Mg + Fe). (B) System Ca-Mg-(Fe + Mn). (C) System Mn-Mg-Fe.

generally low, typically below 1 ppm for V, Co, Ni, Cu, Ag, Sn, Au, and above 10 ppm for Cd, Cr and Zn (Table 5). The highest average concentrations of P, Sc and Ba are in the range of 15–30 ppm, and the Si, Y and Pb concentrations are in the range of 100–200 ppm (Table 5). The highest trace element abundances are those of Sr with 0.013–1.0 wt% (Table 5).

The overall variations in trace element concentration in calcites within individual samples and between the samples are quite high, reaching typically one to two orders of magnitude (in few cases up to three orders of magnitude) (Table 5; Table ST2 in Electronic Supplementary Material). The variations between analyzed grains in many samples exceed also the internal variation within individual grains. The calcites in samples PAM-3a, PAM-18, PAM-31, PAM-80.55

and PAM-51.5 in particular show large compositional variations between analyzed grains (Fig. 7). Mostly the variations within samples do not show a clear pattern, but the calcite data from PAM-3a and PAM-18 show a bimodal distribution corresponding to compositionally different grain populations (Fig. 7). However, the bimodal compositional distribution in these samples is not always observed in all elements, and some elements show a greater compositional overlap between the two grain populations. Besides the overlap observed for certain elements (marked with parentheses in the following), the calcite grains in sample PAM-18 can be grouped according their Mg, Fe, Zn, sr, Pb and (Cd) concentrations and in sample PAM-3a based on their Sr, Zn, Cd, Pb (Fe) and (Y) concentrations (Fig. 7).

Compositional profiles were analyzed in large calcite grains from samples PAM-3a, PAM-9 and PAM-51.5 where no zonation was detected by optical microscopy and CL imaging (Fig. 8). The clearest chemical differences in PAM-3a are visible for Sr and Mn, with concentrations varying in the range of 0.8–1.3 and 0.86–1.0 wt%, respectively (Fig. 8D). In PAM-9, the largest variations are shown by 0.37–0.48 wt% for Mg and 0.42–0.49 wt% for Sr (Fig. 8B), while PAM-51.5 shows very homogeneous trace element compositions for entire calcite crystals (Fig. 8F). Significant variations in Y concentrations are also notable in PAM-3a, with values ranging between 200 and 400 ppm (Fig. 8D). Considerable trace element variations were also detected for the different growth zones visible in CL images in samples PAM-80.55 and PAM-7 (Figs. 9 and 10). In sample PAM-7, the maximum variations between the zones amount to 1000–4000 ppm Mn, 30–900 ppm Sr, 1–20 ppm Y and 10–30 ppm Mg (Fig. 9B to 9D). The concentrations of Sr and Y systematically decrease from the inner zones to the outer rim, while Mn seems to oscillate from one zone to another, having higher concentrations in zones with brighter CL colors (Fig. 9A, 9C and 9D). In sample PAM-80.55, the concentrations of Mn, Sr, Mg and Y show distinct differences between the zones, with variations in the range of 1000–9000 ppm, 30–400 ppm, 10–100 ppm and 0.02–1000 ppm, respectively (Fig. 10B and 10C). The average concentrations of Sr, Mn and Mg appear to be generally higher in the inner zones of the calcite crystals compared to the rims (Fig. 10C and 10D).

The considerable compositional variability of the trace element concentrations in calcite within samples and the overlap between different samples does not make it possible to recognize clear differences between the Pampalo deposit, the Korvilansuo deposit and the Kuittila tonalite. We note that the calcites from hydrothermal veins hosted by the felsic porphyry dikes in the Pampalo and Korvilansuo deposits deposit (PAM-5 and MHS-12) are often compositionally comparable to the calcites in their felsic porphyry host rocks (Fig. 7; Table 5). In the Pampalo deposit, the Y and Mn concentrations in calcites, even though some overlap occurs, reflect the respective host rock lithologies (Fig. 11A and 11B; Table 5) as well. The average Y and Mn concentrations in calcite are lower in the calcites hosted by the mafic (1.5–12.2 ppm Y and 0.47–0.49 wt% Mn) and ultramafic (average 17 ppm Y and 0.5 wt% Mn) metavolcanics than in the calcites hosted by the felsic porphyry dikes (34–93 ppm Y and 0.52–1.14 wt% Mn) and the andesitic metavolcanics (20–220 ppm and 0.47–0.94 wt% Mn). In the Korvilansuo deposit, calcites hosted by the felsic porphyry dike (MHS-12) have somewhat lower Sr and higher Mn concentrations (580 ppm Sr and 0.61 wt% Mn) than the calcites hosted by the metasedimentary host rocks (460 ppm Sr and 0.86 wt% Mn) (Figs. 7 and 11; Table 5).

4.4. REE patterns

The average REE concentrations of the calcites are presented in Table 5; the complete dataset including chondrite-normalized (Boynton, 1984) values are given in the Electronic Supplementary Material (Table ST2). The concentrations of some of the REE, especially the lighter REE, were sometimes below the limit of detection, resulting in incomplete REE patterns for a number of samples. Sample PAM-31 shows greater, up to three orders of magnitude, variations in REE
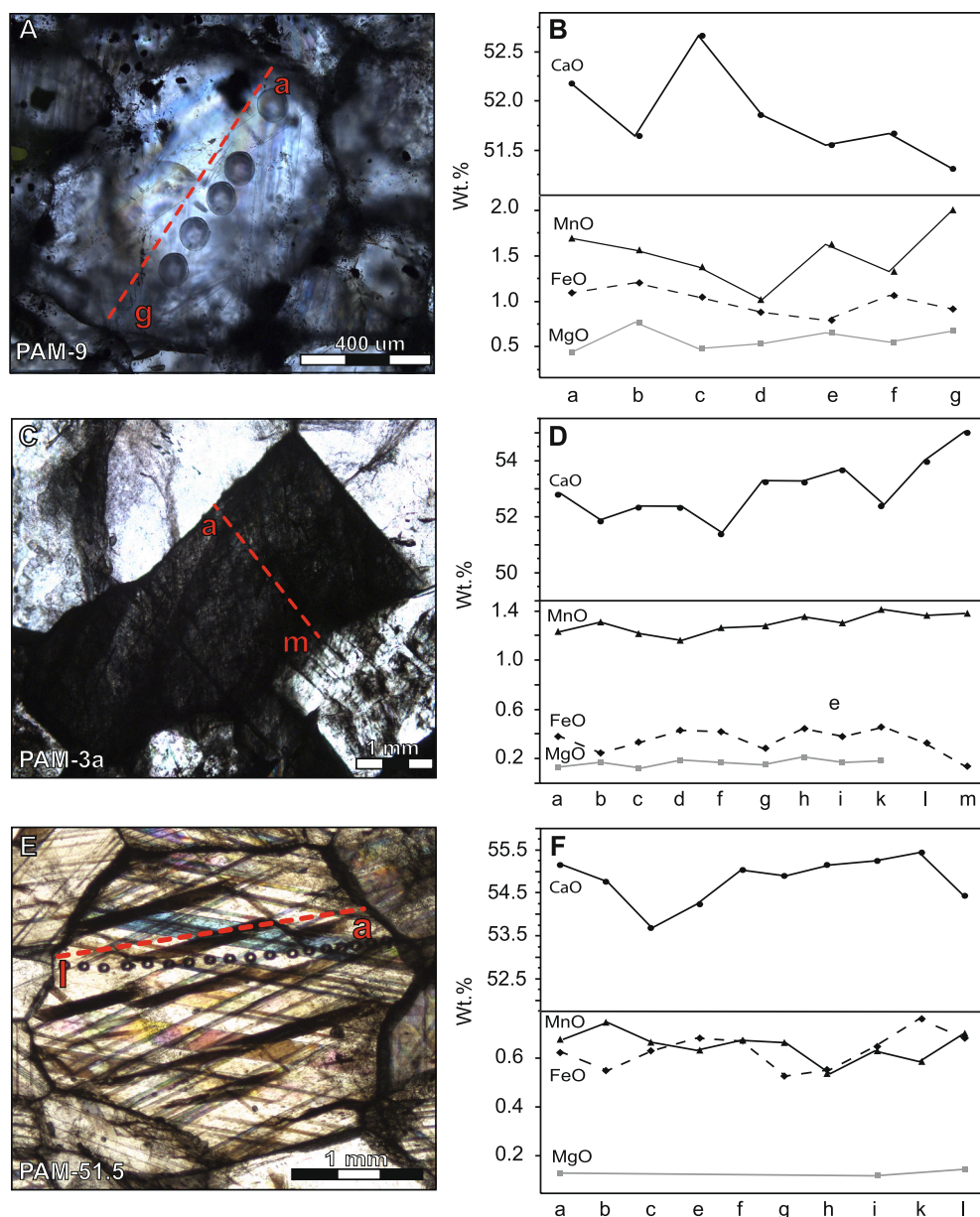
Fig. 6. Photomicrographs and corresponding major element data illustrating the results of EPMA analysis of compositional profiles through hydrothermal calcites from the HSB. The sample spots (small letters on the x-axis of the diagrams in B, D and F) of EPMA analysis are evenly distributed along the profile line highlighted by a red dashed line. The larger black spots visible in the images of (A) and (C) are ablation pits from the LA-ICP-MS analysis. (A) and (B) are hydrothermal host rock calcites from a felsic porphyry dike, (C) and (D) are calcites from a hydrothermal vein sample hosted by the andesitic metavolcanics, and (E) and (F) are calcites from a hydrothermal vein sample hosted by mafic metavolcanics.

concentrations compared to other samples where variations are typically within one order of magnitude. The analyzed calcites show mostly rather similar chondrite-normalized REE patterns with a notable HREE enrichment relative to LREE, although the magnitude of HREE enrichment varies considerably between samples. A few samples (PAM-31, PAM-80.55, PAM-3a and PAE12) shows either flat, slightly concave or slightly LREE to HREE enriched patterns (Fig. 12). While the samples show generally similar REE patterns, some within-grain and intra-sample variations occur. The distinct compositional populations observed in the other trace element data of sample PAM-3A are also visible in their different REE patterns. One calcite population shows a simple linear increase from the LREE to the HREE (Fig. 12H), whereas the second population shows an increase from LREE to MREE and then nearly flat patterns from MREE to HREE (Fig. 12I). The first calcite population with linearly increasing REE has higher Pb, Zn and Cd, but lower Sr concentrations than the second population.

No significant variation in the REE patterns was observed in those samples (PAM-3a, PAM-9 and PAM-51.5) which have no discernible zoning in optical or CL images. However, samples with clearly visible growth zones in the CL images (PAM-80.55 and PAM-7) show distinguishable REE patterns in the different zones (Figs. 13 and 14). From sample PAM-7, two adjacent growth zoned grains were analyzed. In the other grain, outermost overgrowths (zones D, E; Fig. 13) show similar chondrite normalized patters with a linear increase from the LREE to the HREE. In contrast, the inner growth zones have very different REE patterns which almost exclusively show a decrease from the LREE to the HREE, apart from one exception that has flat or concave upwards patterns (zones A, B and C; Fig. 13). The other analyzed grain shows more uniform REE patterns characterized by an increase from the LREE to the HREE between the growth zones (zones H-J; Fig. 13). In sample PAM-80.55, the patterns are flat or show just a moderate enrichment in LREE compared to the HREE in the inner growth zones (zones A and B in Fig. 14A and 14B), while the rims and outer zones shows a distinct LREE enrichment relative to the HREE (zones C-F; Fig. 14A and 14C). Similar patterns of clearly LREE enrichment compared to the HREE are not observed in any other sample investigated, and all other analyzed grains in sample PAM-80.55 show flat REE patterns.

In the Pampalo deposit, the total REE concentrations (ΣREE) can be correlated to specific host rock lithologies, even though some data

Table 5
Representative average trace and rare earth elemental compositions (in ppm) of calcites from the Hattu schist Belt. Abbrevations: b.d. = below the limit of detection, FP = felsic porphyry, AT = andesitic tuff (intermediate volcanic rock), MB = metabasalt (mafic volcanic rock), UM = ultramafic volcanic rock, MS = Mica schist, Ton = tonalite.

Sample	PAM-3a	PAM-10	PAE-12	PAM-51.0	PAM-51.5	PAM-67.7	PAE-9	PAM-9	PAM-18	PAM-31
Host rock	AT	AT	AT	MB	MB	MB	UM	FP	FP	FP
Type	Vein	n/a	Vein	Vein	Vein	Vein	Host rock	Vein	Vein	Vein
Mg	1547.23	2265.71	3661.51	3242.13	836.47	3521.13	4257.62	3442.82	2073.12	72.70
Si	65.27	43.27	109.99	64.75	56.78	52.58	79.51	70.68	53.36	51.57
P	5.47	16.11	15.12	7.18	8.61	7.27	11.77	16.41	7.13	3.60
Sc	9.85	3.02	2.25	2.71	0.15	3.68	31.67	3.35	5.74	0.30
V	0.27	0.01	0.04	0.13	0.30	0.08	0.06	0.02	0.05	0.02
Cr	4.10	4.30	3.85	4.44	3.88	4.45	4.71	3.99	4.19	4.02
Mn	9425.52	6358.41	4682.92	4649.78	4904.73	4819.45	4995.24	7272.79	9608.39	5283.33
Fe	4234.57	5942.74	4708.43	8788.10	4730.11	7068.66	6424.90	6534.47	6913.98	304.94
Co	0.04	0.58	0.05	0.70	0.18	0.45	0.09	0.11	0.15	0.03
Ni	0.25	0.50	0.46	0.21	0.19	0.21	0.35	0.32	0.23	0.19
Cu	0.08	0.05	0.05	0.02	0.02	0.01	0.02	0.04	0.03	0.02
Zn	3.31	4.10	1.89	1.40	1.72	1.66	1.33	6.01	4.46	0.13
Sr	9520.65	6647.44	2718.76	163.40	137.62	356.41	2012.59	4835.16	3273.02	170.03
Y	213.96	100.92	20.32	5.49	1.48	12.18	17.41	92.69	50.03	34.23
Ag	0.01	0.01	0.02	b.d.	0.01	b.d.	b.d.	b.d.	0.01	b.d.
Cd	0.83	1.06	0.64	0.46	0.20	0.59	2.36	1.57	3.33	0.11
Sn	0.01	0.01	0.02	0.01	0.01	0.01	0.01	0.02	0.01	0.02
Ba	10.40	3.38	24.25	1.20	1.66	3.61	12.53	2.72	1.49	0.04
Pb	23.50	89.49	56.02	4.00	3.60	15.50	20.64	85.81	36.56	0.01
REE										
La	5.07	1.55	11.73	0.01	0.00	0.05	0.29	1.49	0.59	18.19
Ce	16.70	3.94	25.10	0.03	0.01	0.19	0.79	4.00	1.69	44.98
Pr	2.94	0.64	3.05	0.01	0.00	0.04	0.13	0.64	0.27	5.45
Nd	17.77	3.83	12.64	0.05	0.01	0.27	0.63	3.45	1.72	17.07
Sm	10.16	2.00	2.25	0.04	0.01	0.18	0.38	1.47	0.82	4.91
Eu	5.28	0.88	0.60	0.10	0.03	0.07	0.41	0.83	0.43	1.53
Gd	21.32	5.17	2.13	0.12	0.04	0.46	1.19	3.29	1.80	5.26
Tb	3.84	1.23	0.27	0.03	0.01	0.12	0.26	0.87	0.39	1.04
Dy	24.91	10.69	1.86	0.32	0.11	1.16	2.37	8.36	3.59	4.91
Ho	4.77	2.73	0.51	0.11	0.04	0.36	0.72	2.37	1.17	0.96
Er	12.83	9.45	1.95	0.58	0.15	1.48	2.77	8.62	5.08	2.22
Tm	1.60	1.42	0.33	0.14	0.03	0.27	0.44	1.36	0.97	0.32
Yb	9.19	9.37	2.79	1.75	0.21	2.55	3.44	9.33	8.31	1.74
Lu	1.07	1.25	0.55	0.45	0.03	0.77	0.60	1.22	1.60	0.23
ΣREE	137.45	54.15	65.76	3.75	0.68	7.98	14.41	47.31	28.41	108.81
(La/Lu)N	0.49	0.13	2.21	0.00	0.01	0.01	0.05	0.13	0.04	8.24
Eu/Eu*	1.10	0.84	0.84	4.30	4.06	0.74	1.85	1.15	1.09	0.92
Ce/Ce*	1.04	0.96	1.01	0.86	0.73	1.02	0.98	0.99	1.03	1.09

Sample	PAM-80.55	PAM-5	PAM-5	PAM-15	PAM-7	MHS-12	MHS-12	MHS-10b	KUI-1
Host rock	FP	FP	FP	FP	Unknown	FP	FP	MS	TON
Type	vein	Vein	Host rock	Vein	Vein	Host rock	Vein	Vein	Host rock
Mg	824.35	2181.22	2243.90	1661.70	417.90	1934.76	1922.59	1877.39	3606.47
Si	45.55	62.50	76.36	109.27	75.72	109.91	71.91	59.03	80.72
P	4.25	11.55	10.64	13.43	5.67	7.71	6.87	6.54	15.28
Sc	20.27	0.47	0.45	0.79	4.04	1.07	1.99	0.83	0.89
V	0.17	0.02	0.02	0.04	0.04	b.d.	0.02	0.03	0.02
Cr	4.20	4.59	4.43	4.25	4.12	4.29	4.24	4.30	4.59
Mn	9103.96	11366.82	10865.96	7411.33	8310.39	6140.52	6075.11	8593.20	6039.97
Fe	2429.22	6040.49	6108.47	7384.92	3035.60	3727.12	3695.27	4938.70	6372.30
Co	0.02	0.02	0.02	0.06	0.03	0.11	0.10	0.17	0.51
Ni	0.17	0.21	0.24	0.23	0.17	0.19	0.18	0.20	0.27
Cu	0.04	0.02	0.01	0.04	0.03	0.03	0.02	0.02	0.03
Zn	0.20	6.18	6.53	3.48	0.77	2.09	1.92	2.58	1.94
Sr	5852.36	1054.73	984.20	1069.16	2022.30	581.37	575.37	460.23	525.90
Y	81.41	58.11	56.99	92.99	48.44	10.99	11.58	8.13	59.92
Ag	0.01	0.01	b.d.	b.d.	b.d.	0.01	b.d.	b.d.	b.d.
Cd	0.08	1.09	1.20	1.46	0.49	2.66	2.31	4.75	1.19
Sn	0.02	0.02	0.01	0.02	0.03	0.02	0.02	0.02	0.02
Ba	2.35	0.41	0.55	2.21	0.94	3.45	3.82	3.07	1.86
Pb	0.60	27.56	27.25	47.88	7.59	15.19	14.69	18.66	15.19
REE									
La	9.05	0.70	1.01	1.92	2.49	0.05	0.15	0.02	0.03
Ce	15.41	1.81	2.50	4.14	5.69	0.14	0.34	0.05	0.11
Pr	1.88	0.30	0.36	0.57	0.72	0.02	0.06	0.01	0.04
Nd	8.43	1.85	1.99	2.82	3.43	0.20	0.38	0.06	0.42
Sm	4.23	1.02	0.99	1.25	1.52	0.13	0.19	0.04	0.40
Eu	1.76	0.48	0.48	0.60	0.61	0.06	0.08	0.03	0.15
Gd	7.35	2.29	2.22	2.66	2.83	0.36	0.41	0.11	1.43

(*continued on next page*)

Table 5 (*continued*)

Sample	PAM-80.55	PAM-5	PAM-5	PAM-15	PAM-7	MHS-12	MHS-12	MHS-10b	KUI-1
Host rock	FP	FP	FP	FP	Unknown	FP	FP	MS	TON
Type	vein	Vein	Host rock	Vein	Vein	Host rock	Vein	Vein	Host rock
Tb	1.42	0.48	0.48	0.64	0.69	0.08	0.09	0.03	0.40
Dy	9.38	4.12	4.11	6.50	5.11	0.81	0.84	0.45	4.60
Ho	1.91	1.25	1.23	2.11	1.33	0.27	0.27	0.18	1.64
Er	5.47	5.20	5.00	9.54	4.94	1.16	1.25	1.10	7.38
Tm	0.74	0.90	0.84	1.71	0.92	0.22	0.24	0.27	1.42
Yb	4.70	7.07	6.71	12.75	7.81	2.05	2.23	2.71	11.96
Lu	0.57	1.15	1.08	1.80	1.50	0.46	0.52	0.52	2.05
ΣREE	72.28	28.63	29.02	49.00	39.57	6.02	7.05	5.59	32.04
$(La/Lu)_N$	1.65	0.06	0.10	0.11	0.17	0.01	0.03	0.00	0.00
Eu/Eu*	0.96	0.95	0.99	1.01	0.90	0.82	0.88	1.26	0.59
Ce/Ce*	0.90	0.95	0.99	0.95	1.03	1.00	0.85	0.95	0.78

overlap is observed (Fig. 15A). The lowest average ΣREE concentrations in calcite are 0.68–8.0 ppm and these calcites are hosted by the mafic metavolcanic rocks (Table 5; Fig. 15A). Ultramafic host rocks have just slightly higher ΣREE of about 14 ppm on average (Table 5; Fig. 15A). The data of calcites from the andesitic metavolcanics and felsic porphyry dikes of the Pampalo deposit show largely overlapping ΣREE concentrations in the range of 28 to 140 ppm (Table 5; Fig. 15A). In the Korvilansuo deposit, the ΣREE of hydrothermal calcites from the mica schists and felsic porphyry dikes are in the same range of 5.6–7.1 ppm, and these values are similar to calcites in the mafic host rocks of the Pampalo deposit (Table 5; Fig. 15A). The calcites from the Kuittila tonalite, on the other hand, have average ΣREE values of 32 ppm, which are close to those of the calcites from felsic porphyry dikes and andesitic metavolcanics in the Pampalo deposit (Table 5; Fig. 15A). The relative fractionation of the REE, as described by the chondrite-normalized La/Lu ratios, i.e. $(La/Lu)_N$, shows differences between the different host lithologies in the Pampalo deposit as well. The average $(La/Lu)_N$ values are < 0.01 in calcites in the mafic metavolcanics of the Pampalo deposit, while in the ultramafic metavolcanics the $(La/Lu)_N$ values are around 0.05. In contrast, the $(La/Lu)_N$ ratio is distinctly higher in the andesitic tuffs and felsic porphyry dikes with the average values ranging between 0.04 and 8 (Table 5; Fig. 15B). Finally, the $(La/Lu)_N$ ratios of disseminated and vein calcites in the felsic dikes of the Korvilansuo deposit and in the Kuittila tonalite are largely comparable to those of the calcites in the mafic metavolcanics of the Pampalo deposit (Table 5; Fig. 15B).

The europium anomaly (Eu/Eu*), defined as $Eu_N/(\sqrt{Sm_N * Gd_N})$, is only weakly developed or lacking in most of the samples investigated, except in calcites from the Pampalo mafic metavolcanics (PAM-51.0 and PAM51.5) where most calcites show a rather large Eu anomaly reaching average values of 4 (Fig. 12; Table 5). The calcites from ultramafic metavolcanics of the Pampalo deposit have average Eu/Eu* ratios of 1.9, which also are slightly higher than in the remainder of the samples where the average Eu/Eu* ratios are always < 1.3. The two samples with the highest Eu/Eu* ratios (PAM-51.0 and PAM-51.5) are showing the lowest ΣREE concentrations. Cerium anomalies (Ce/Ce*), defined as $Ce_N/\sqrt{(La*Pr)_N}$, are only weakly developed in the REE patterns of the hydrothermal and host rock calcites, which have average Ce/Ce* ratios between 0.7 and 1.03. (Fig. 12; Table 5).

5. Discussion

5.1. Geochemical implications

A number of elements, such as Mg, Mn, Sr, Y and some of the REE, can be incorporated into carbonate minerals by different processes including crystal-chemical substitution and surface adsorption (e.g. McIntire, 1963; Veizer, 1983 and references therein; Zhong and Mucci, 1995). The element partitioning between hydrothermal fluids and calcite is affected by several additional factors, including the composition

of the hydrothermal fluid, the flow rates of the fluid, pressure–temperature conditions, and the calcite precipitation rates (e.g. Lorens, 1981; Lahann and Siebert, 1982; Mucci and Morse, 1983; Veizer, 1983; Möller et al., 1991; Tesoriero and Pankow, 1996; Gabitov et al., 2014; Voigt et al., 2017). The REE partitioning between fluids and calcites is, however, mainly controlled by variations in the REE composition of the hydrothermal fluids (e.g. Zhong and Mucci, 1995; Voigt et al., 2017). Other factors such as the concentration of CO_3^{2-}, the P_{CO2} or the precipitation rate, are somewhat less important, as shown by the experimental studies of Terakado and Masuda (1988) and Zhong and Mucci (1995). In addition, the experiments of Zhong and Mucci (1995) demonstrated that the fluid-calcite partition coefficients of the REE decrease systematically with the atomic number when their concentration in solution is constant.

In calcites, the REE abundances, their fractionation and the Eu and Ce anomalies are not only reflecting the physico-chemical environment of deposition but also the chemical properties of the fluid (Bau and Möller, 1992). In particular, variations in the REE concentrations of hydrothermal calcites could indicate variations in fluid chemistry, as the partitioning of the REE between fluid and crystallizing calcite is mainly reflecting the variations in fluid composition (e.g. Terakado and Masuda, 1988; Zhong and Mucci, 1995; Voigt et al. 2017). In contrast, Eu and Ce anomalies are indicative of changes in the oxidation state in the hydrothermal environment (Bau and Möller, 1992; Bau, 1991). Despite the considerable potential of hydrothermal calcites for reconstructing key parameters of the ore-forming environment, only a limited number of trace element and REE studies of ore-related calcites have been performed (e.g. Möller et al., 1979, 1984; Kontak and Jackson, 1995, 1999; Barker et al., 2006; Fusswinkel et al., 2013), with even fewer data for hydrothermal calcites from orogenic gold deposits (e.g. Sarangi et al., 2013; Dubinina et al., 2014; Hazarika et al., 2016).

The concentrations of many trace elements in the hydrothermal calcites from the HSB are rather low, and the data for many sample types and populations (such as calcites from different host rock lithologies or successive hydrothermal vein generations) show considerable overlap (Table 5; Fig. 7). Reported trace elemental concentrations in calcites related to hydrothermal ore deposits elsewhere are also generally low, except for Sr which can become considerably enriched (e.g. Kontak and Jackson, 1999; Fusswinkel et al., 2013). The notable enrichment of Sr is also evident in the hydrothermal calcites of the HSB where Sr (along with Mn, Fe and Mg) can reach concentrations up to about 1.0 wt% (Tables 4 and 5). Despite considerable trace element variation and compositional overlap in the hydrothermal calcites of the HSB, the data nevertheless permit to interpret them qualitatively in terms of fluid composition and effects of fluid-rock reaction with different host rock lithologies.

5.1.1. Effect of multiple fluid events on trace element variation in calcite

Most minor and trace element concentrations in the hydrothermal calcites from the HSB are rather low and show broad variations within
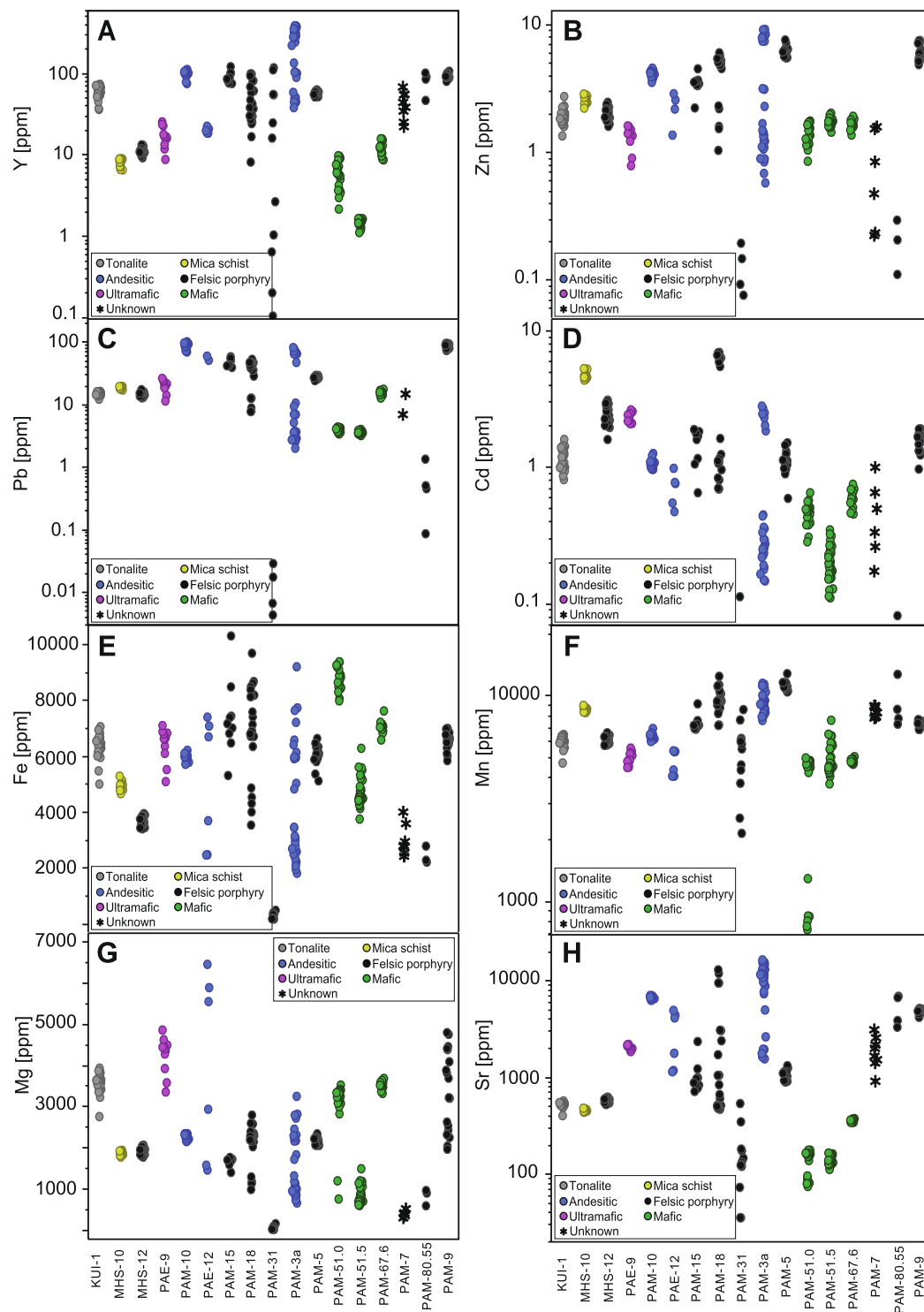
Fig. 7. Summary plot of the major and trace element composition of hydrothermal calcites from the Hattu schist belt, showing the concentrations of (A) Y, (B) Zn, (C) Pb, (D) Cd, (E) Fe, (F) Mn, (G) Mg, and (H) Sr analyzed with LA-ICP-MS.

samples and even at the scale of individual grains (Figs. 7–10). In contrast, the REE show uniform patterns within most samples and within crystals (Fig. 12), even though few exceptions of REE zoned crystals occur (Figs. 13 and 14). CL imaging revealed that in some grains, especially close to fractures and grain boundaries, areas with differing CL intensities are present. This is probably due to small-scale fluid-induced alteration or irregularities in physical topography of the grain, however our data do not allow to correlate these areas to specific

elemental variations. Furthermore, EPMA and LA-ICP-MS analysis of compositional profiles (e.g. samples PAM-51.5 and PAM-9) revealed that some calcite crystals or grains which have no growth zoning or those irregularities visible in CL described above can nevertheless show trace element variations by up to tens (Y) or even thousands (Sr, Mn, Mg, Fe) of ppm (Figs. 6 and 8). This may indicate that the chemical zoning is caused by a group of elements which are not efficient cathodoluminescence activators, or where the CL intensities are not
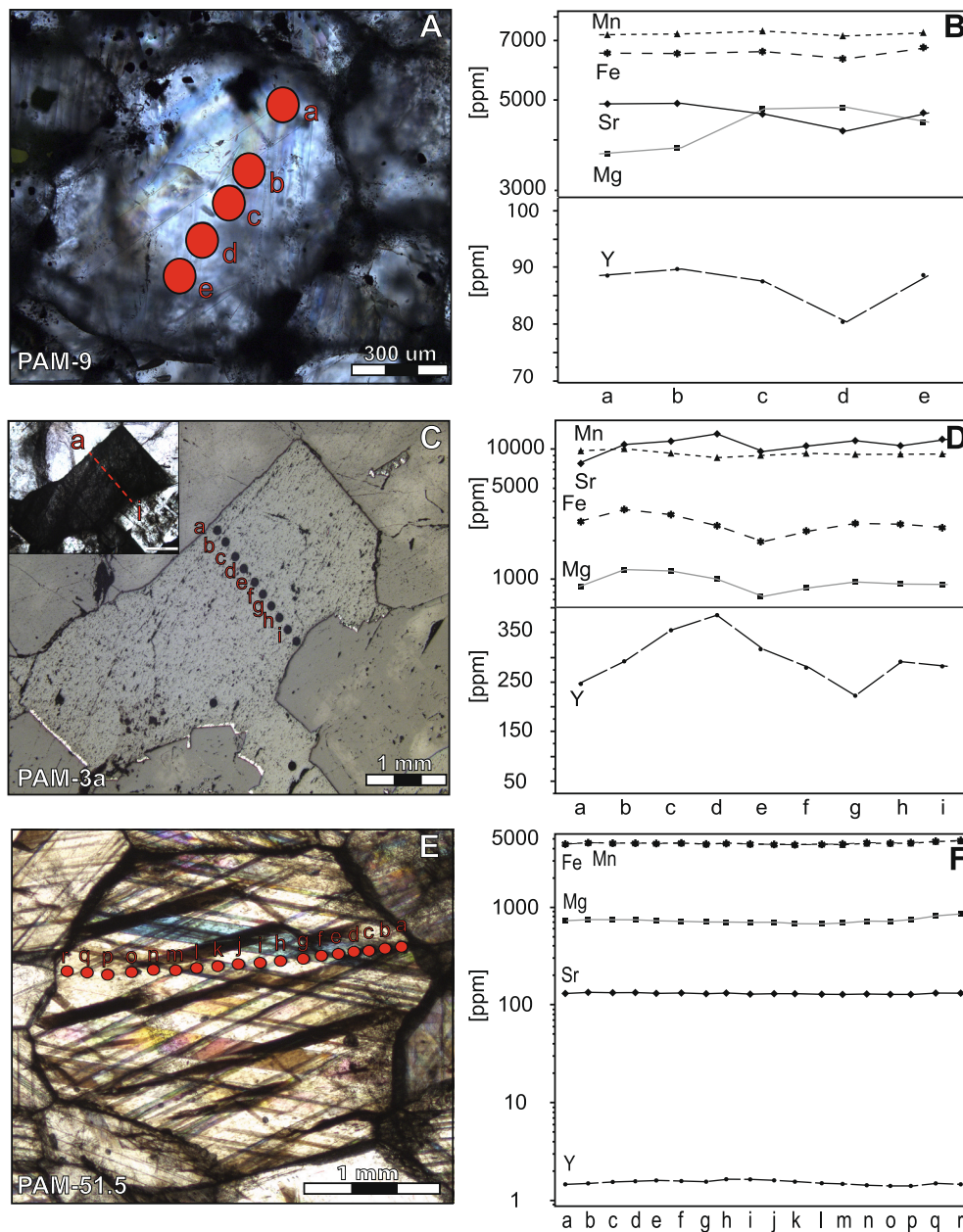
Fig. 8. Photomicrographs and corresponding trace element data illustrating the results of LA-ICP-MS analysis of compositional profiles through hydrothermal calcites from the HSB. These calcite samples did not show any visible zoning or intensity variations in CL imaging. (A) and (B) are from a calcite bearing felsic porphyry dike (PAM-9), (C) and (D) are from a hydrothermal vein (PAM-3a) hosted by the andesitic metavolcanics, and (E) and (F) are from a hydrothermal vein (PAM-51.5) hosted by the mafic metavolcanic host rocks.

sensitive enough to variations in the concentrations of these elements. Even apparently homogenous carbonate crystals are known to contain complex intergrowths and discrete structural domains that may also influence the internal chemistry of individual crystals (Veizer, 1983 and references therein). For example, it has been suggested that the structural configuration of calcite crystals controls the growth and trace elemental incorporation, which leads to heterogeneities in the bulk chemistry of the crystals (e.g. Paquette and Reeder, 1995; Reeder, 1996). Effects of such small-scale crystal-chemical control could at least partly explain the considerable variation of trace element concentrations at the scale of individual crystals even where optical or CL zoning features were not detectable.

The cathodoluminescence of carbonates is mainly controlled by the concentrations of Fe and Mn, while other trace elements including Zn and Pb, at least when present at low concentrations, do not activate the

CL or affect its intensity (e.g. Fairchild, 1983; Budd et al., 2000). Compositionally different calcite populations recognized in samples PAM-3a and PAM-18 do not show differences in their CL intensities, whereas the important control of Mn on CL intensities in calcite is shown by the strongly growth zoned calcite samples PAM-7 and PAM-80.55. Here, the zones with high CL intensity (orange/yellowish in color) correlate with higher Mn concentrations (up to several thousands of ppm), whereas zones with lower Mn concentration show much lower CL intensities (deep red in color) (Figs. 9 and 10). Conversely, the concentrations of Fe could not be correlated with differences in the CL intensities.

Although intrinsic crystal-chemical controls can affect trace element incorporation into calcite, we nevertheless find it difficult to explain the full compositional and textural spectrum of hydrothermal calcites in crustal-scale hydrothermal systems such as the HSB by these effects
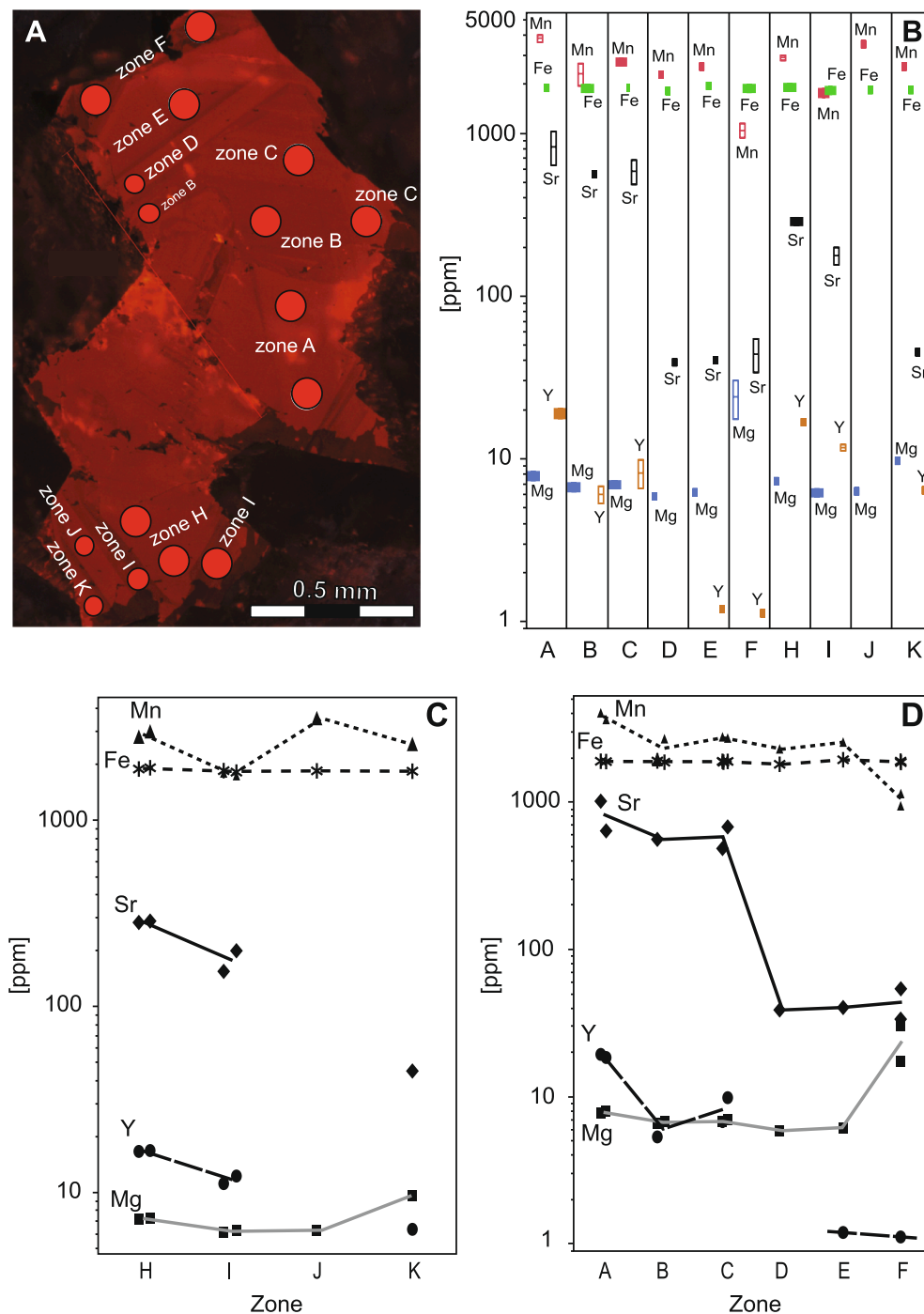
Fig. 9. Cathodoluminescence image and plots of compositional data, illustrating the results of LA-ICP-MS trace element profile analysis for the strongly zoned hydrothermal calcites of sample PAM-7. (A) Cathodoluminescence image showing the complexly zoned calcite crystals. Red circles highlight the LA-ICP-MS spots analyzed and the upper-case letters label the different texturally distinguishable growth zones. (B) Boxplot diagram showing average compositions and the variations of Sr, Mn, Y, Mg and Fe in each of the representative growth zones. (C) Compositional profiles for Sr, Mn, Y, Mg and Fe in growth zones H to K. (D) Compositional profiles for Sr, Mn, Y, Mg and Fe in growth zones A to F.

alone. Rather, the large variations of trace element and REE concentrations in the hydrothermal calcites of the HSB, which are often related to primary growth zoning, should reflect successive changes in fluid composition and pressure–temperature conditions during calcite precipitation. The experimental data of Zhong and Mucci (1995) and Voigt et al. (2017) show that the partitioning of the REE between fluid and calcite is strongly dependent on the REE chemistry of the aqueous fluid. Accordingly, the presence of different types of REE patterns (and the covariation of Pb, Zn, Cd and Sr with the REE) in two calcite populations in sample PAM-3a (Fig. 12) most likely reflects changes in fluid compositions, related to the successive influx of compositionally different fluid pulses. Similarly, the variation of the REE compositions of calcites from auriferous quartz veins in the Phanerozoic metaturbidite hosted orogenic gold deposits of the Meguma terrane in Nova

Scotia (NE Canada) (Kontak and Jackson, 1999) and unmineralized hydrothermal veins from the low-grade metamorphic Cavan Bluff Limestone of the Lachlan Orogen, southeast Australia (Barker et al., 2006) has been attributed, at least partly, to the changes in fluid composition.

While most calcite samples from the HSB show intra-crystal variations in trace element concentrations, they rarely show well-developed growth zoning that can be detected with CL. Notable exceptions are calcite crystals in samples PAM-7, PAM-80.55 and PAM-51.0, which show clear growth zoning in CL (Figs. 4A, 4C, 4E, 9A, 10A). The concentrations of Sr, Y and Mn show variations from core to the outer rims, with clear changes between individual growth zones. The development of compositional zonation has been attributed to a number of different factors such as calcite growth rate (e.g. Barker and Cox, 2011), effects
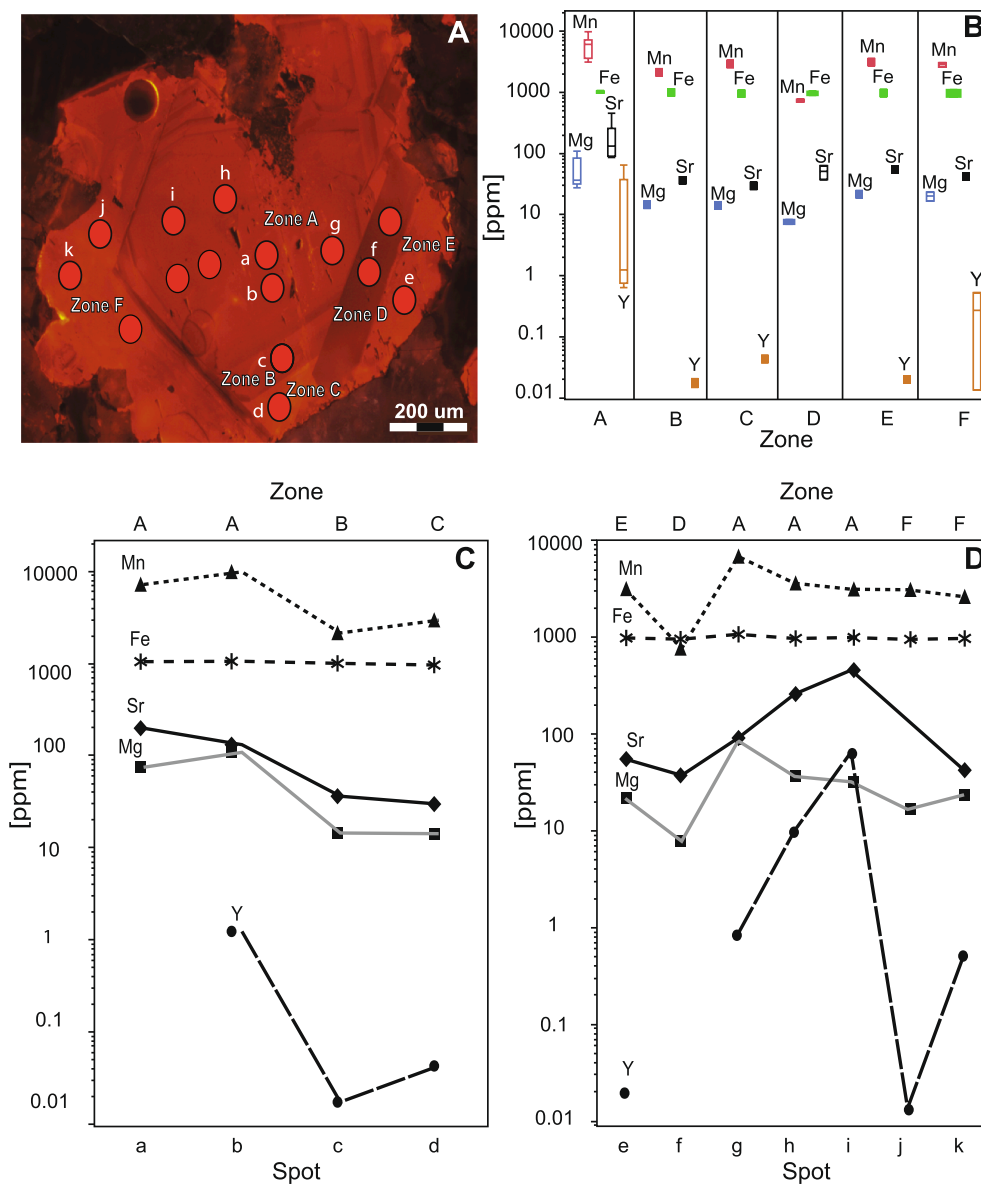
Fig. 10. Cathodoluminescence images and plots of compositional data, illustrating the results of LA-ICP-MS trace element profile analysis for the strongly zoned hydrothermal calcites of sample PAM-80.55. (A) Cathodoluminescence image showing the complexly zoned calcite crystals. Red circles with lower case letter highlight the LA-ICP-MS spots analyzed and the upper-case letters label the different texturally distinguishable growth zones. (B) Boxplot diagram showing average compositions and the variations of Sr, Mn, Y, Mg and Fe in each of the respective growth zones. (C) Compositional profiles for Sr, Mn, Y, Mg and Fe in growth zones A to C (spots a-d). (D) Compositional profiles for Sr, Mn, Y, Mg and Fe in growth zones A to F (spots e-k).

of crystal and surface structures (e.g. Reeder and Grams, 1987; Paquette and Reeder, 1990), and changes in fluid composition (e.g. Wogelius et al., 1997). The exact mechanism dominating the development of detectable growth and chemical zonation in the HSB calcites cannot be identified with the current data. However, considering that in the HSB several generations of hydrothermal veins containing calcites are present (Fusswinkel et al., 2017) and that the vein-hosted hydrothermal calcites have chemically distinct (Fe, Mg, Pb, Zn, Co, Cd and Sr and REE patterns) populations of grains without apparent growth zoning (Figs. 7 and 12), we interpret the strongly growth zoned calcite crystals (samples PAM-7, PAM-80.55 and PAM-51.0) in terms of introduction of and growth from successive fluid pulses with chemical differences. This interpretation is consistent, at least in sample PAM-7, with 1) the presence of galena, which has been interpreted as a late phase in the HSB ore mineral paragenesis (Kojonen et al., 1993) and 2) the LA-ICP-MS data of fluid inclusions which demonstrate clear differences in fluid composition for the three successive hydrothermal vein generations, of which the galena and zoned calcite bearing veins (sample PAM-7) represent the youngest generation (Fusswinkel et al., 2017). In addition, the observed zonation of calcite is a very local feature in the HSB veins, which could be explained by localized fluid flow. If some intrinsic crystal-chemical control or gradients in P-T conditions would have been

responsible for the growth zoning, all analyzed hydrothermal calcites of the HSB should be growth-zoned, which is clearly not the case.

The data do not permit to directly correlate the trace element chemistry of calcites with the chemical changes of the hydrothermal fluid as established by the fluid inclusion study of Fusswinkel et al. (2017). This is because the trace element data show considerable variability and overlapping of chemical compositions between and within the calcite samples. Nevertheless, some chemical features are apparent, where the trace element chemistry of the hydrothermal calcites corresponds well to the directly measured fluid chemistry. For example, in the early vein type (PAM-80.55) the core parts of the zoned calcite grains have higher Sr compositions than the outer growth zones and rims (Fig. 10), which agrees well with the observation that Sr concentrations are much higher in fluid inclusions from the early hydrothermal vein generation (fluid inclusion type B; Fusswinkel et al., 2017) than in those from the later generations (fluid inclusion types C-E; Fusswinkel et al., 2017). Similarly, the core parts and the outer growth zones in the calcite grains of the late vein type (PAM-7, Fig. 9) and the two compositionally different calcite populations in sample PAM-3 have contrasting Sr concentrations, which probably reflects formation from the compositionally different fluid types. The higher Sr concentrations in the fluid inclusions from the early vein type most
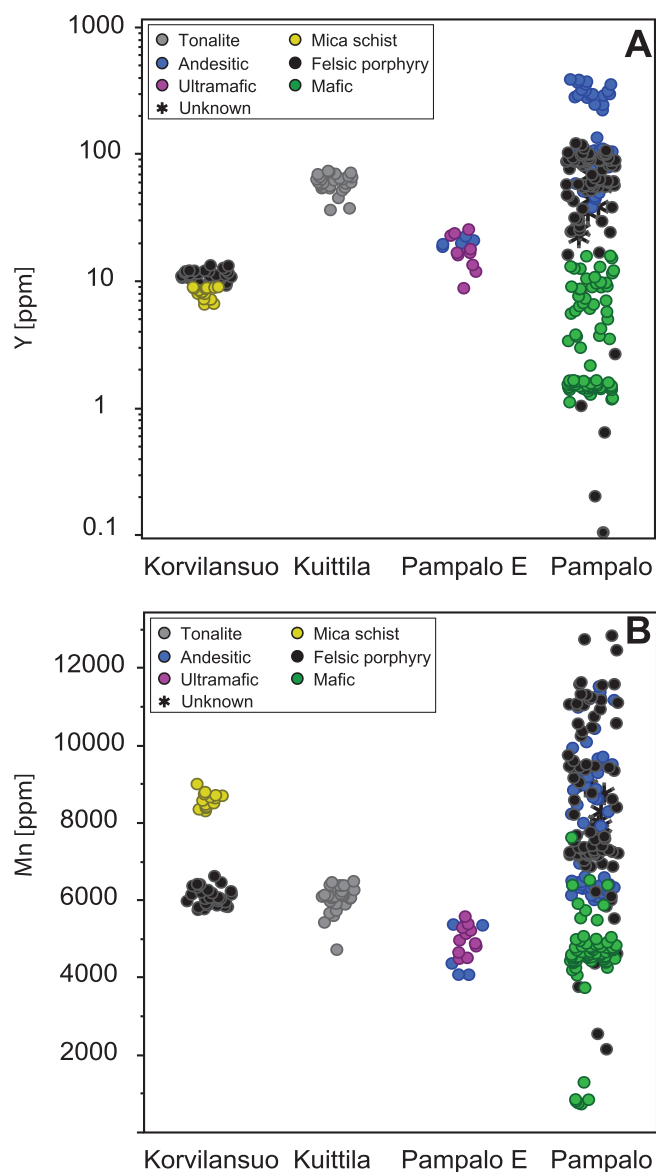
Fig. 11. Summary plots of the (A) Y and (B) Mn concentrations of calcites from the HSB, classified according to locality and host rock lithology.

likely reflect interaction of the ore mineralizing fluid with Ca-richer lithologies (Fusswinkel et al., 2017).

5.1.2. Calcite composition dependence on host rock lithologies

One of the most important features of the HSB calcites is the systematic variation of the elemental composition as function of the respective host rock lithologies. In the Korvilansuo deposit, the calcites hosted by felsic porphyry dikes (sample MHS-12) have higher Sr concentrations and lower Mn compared to calcites hosted by metasedimentary mica schists (sample MHS-10b) (Figs. 7 and 11B; Table 5). The chemical differences of Sr in calcite resemble those observed for the bulk composition of the respective host rocks. The range of whole-rock bulk Sr concentrations of felsic porphyry dikes in the HSB is higher (595–700 ppm) compared to that of the metasedimentary rocks (230–590 ppm) (whole-rock geochemical data from Bornhorst et al., 1993). Furthermore, the trace element compositions of hydrothermal vein calcites and of disseminated calcites in the felsic porphyry dike of the Korvilansuo and Pampalo deposits are essentially the same (Fig. 7; Table 5), demonstrating the importance of fluid-rock interaction with local host rocks in controlling calcite chemistry. In the Pampalo deposit,

the Mn, Y, ΣREE and (La/Lu)$_N$ compositions of hydrothermal calcites vary systematically between different host rock lithologies and are all lower in mafic metavolcanics compared to the andesitic metavolcanics and felsic porphyry dikes (Figs. 11 and 15). This is evidence for a host rock buffering effect on fluid chemistry and calcite composition and highlights that the trace element chemistry of hydrothermal calcites cannot be directly used as a first-order proxy for the distal fluid sources. In the Pampalo East deposit, the correlation between the Mn and Y concentrations of calcite and different host lithologies is not as clear, because the data for calcites from the andesitic (PAE-12) and ultramafic (PAE-9) host rock overlap. However, sample PAE-9 comes from a zone in the deposit which is located close to the contact between these two lithological units, suggesting that the hydrothermal fluid may have partly interacted with both rock types, leading to a mixed signal in the calcite trace element data.

The Y, Sr, and Mn concentrations show a positive correlation with increasing ΣREE. The data for calcites from different host rock lithologies do clearly cluster, and the data show that the andesitic metavolcanics on one end of the trend are separated from the mafic metavolcanics on the other end, even though some data overlap is observed (Fig. 16). This shows that some of the trace elements behave similar to the ΣREE and that the bulk composition of different host rocks at least partly buffers the local fluid composition. Conversely, the chemically distinct growth zones and compositional populations in certain samples cannot be explained by the effect of local host rock control and rather demonstrate multiple successive fluid events causing formation of calcite with different compositions. Taken together, the calcites from the HSB record signals from compositionally different fluid generations as well as fluids interacting with diverse local host rocks, a conclusion which may apply to hydrothermal calcites from other orogenic gold deposits with similar diverse host rock lithologies and hydrothermal history elsewhere.

5.1.3. REE as proxies for changes in the calcite depositional environment

The analyzed calcites from the HSB show low REE abundances and mostly uniform chondrite normalized patterns with LREE depletion and HREE enrichment (Fig. 12; Table 5). The REE fractionation varies somewhat between different samples and a few calcites (PAM-31, PAM-80.55, PAE-12, PAM-3a) have almost flat, slightly concave REE patterns or patterns which show very minor LREE enrichment relative to the HREE (Fig. 12). Only the growth zoned calcites (PAM-7 and PAM-80.55) have also individual zones or LA-ICP-MS spot analysis with reversed REE patterns which show distinctively LREE enrichment relative to the HREE. In contrast to the majority of hydrothermal calcites, which are characterized by HREE enriched patterns, the bulk rock REE data of different host rocks in the HSB show mostly patterns with LREE enrichment relative to the HREE and variable degrees of REE fractionation (see O'Brien et al., 1993). The relative magnitude of the fractionation depends on the host rock lithology, with felsic metavolcanics and intrusives showing high LREE over HREE fractionation, whereas the patterns of mafic metavolcanics are almost flat or just weakly LREE enriched. None of the host rock lithologies in the HSB shows a pattern of HREE (or MREE) enrichment relative to the LREE which would resemble those of the hydrothermal calcites. This suggests that although the ΣREE content and La/Lu$_N$ ratio of the hydrothermal calcites correlate with those of the respective host rock lithologies, the REE fractionation is not controlled by fluid-rock interaction and the chemistry of different host rocks but its rather a feature inherited from the fluid.

Hydrothermal quartz vein hosted carbonates (ankerites) with low REE concentrations and REE patterns which show enrichment of HREE over the LREE, similar to those from the HSB, have already been described from the metasediment hosted hydrothermal-metamorphic Sukhoi Log gold deposit in Russia (Dubinina et al., 2014). The REE patterns of these hydrothermal vein carbonates have been interpreted as mainly being inherited from fluids derived from the metamorphic country rocks. None of the hydrothermal calcites in the HSB (with the
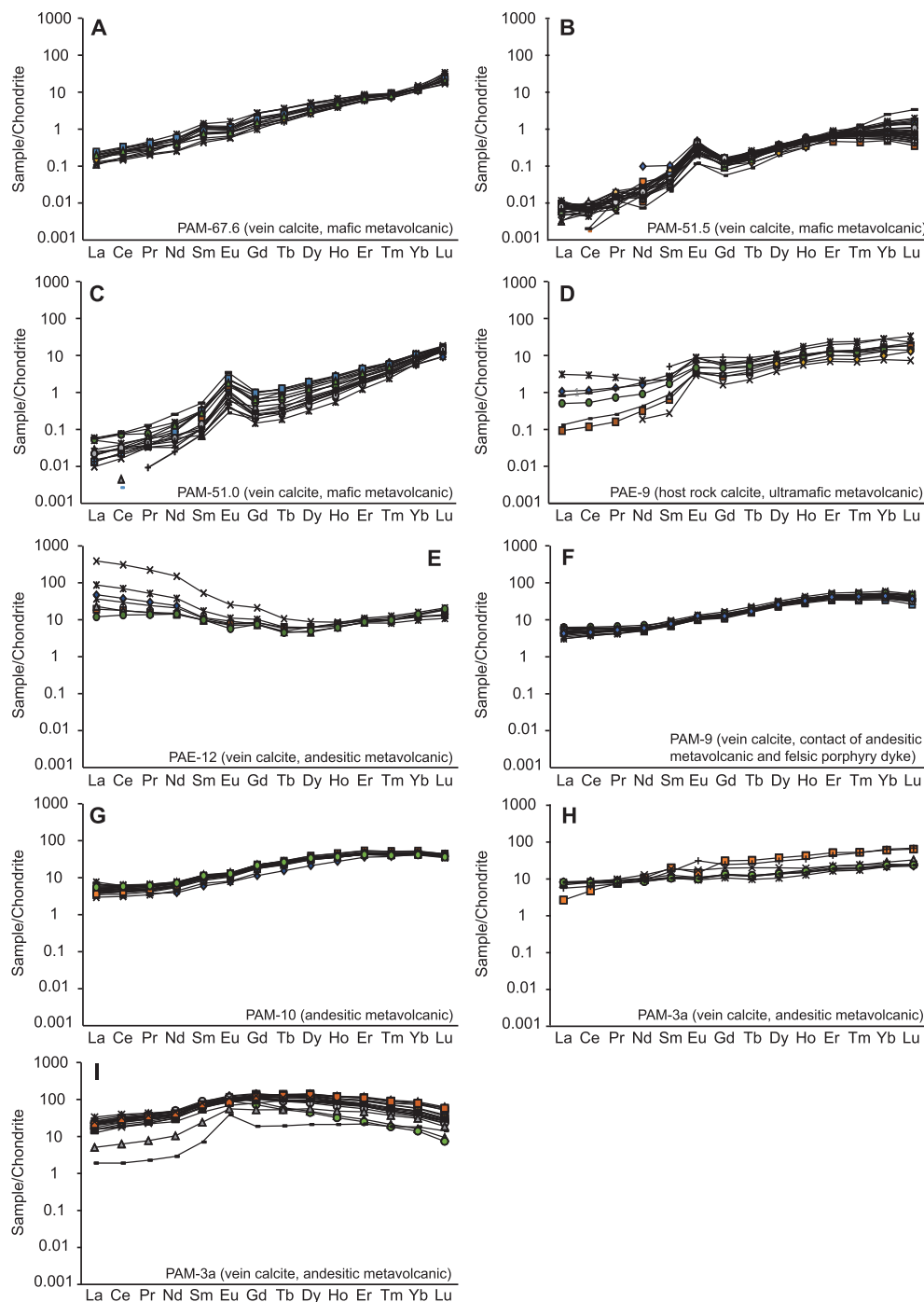
Fig. 12. Chondrite normalized (Boynton, 1984) REE patterns of calcites of the HSB from (A-I) metavolcanic host rocks and (J-R) felsic porphyry dikes, tonalites and mica schists.

exception of spots analyzed from the zoned calcites in samples PAM-7 and PAM-80.55), including those hosted by felsic porphyry dikes and tonalite intrusions, show high REE concentrations with strongly fractionated patterns with LREE enrichment and HREE depletion, which are more typical for calcites related to magmatic-hydrothermal environments (e.g. Möller et al., 1979). This suggests that in the HSB the hydrothermal fluids precipitating the calcites, and evidently the gold ore stage fluids as well, have a predominantly metamorphic origin. This confirms the results of LA-ICP-MS analysis of fluid inclusions related to the main gold ore stage and mass balance modeling, which have demonstrated that the orogenic gold mineralizing system of the HSB was mainly driven by fluids of metamorphogenic origin, whereas

contributions from magmatic fluids were rather insignificant (Fusswinkel et al., 2017).

The calcites of the HSB shows almost exclusively $(La/Lu)_N < 1$ (Table 5; Fig. 15B), which, in the absence of host rock effects, can be explained by fluid complexation controlling fluid-calcite partitioning (Bau, 1993). Calcite precipitation from fluids enriched in dissolved carbonate and bicarbonate, which both form stronger complexes with the HREE than with LREE, would be consistent with the observed REE data because such fluids preferentially mobilize HREE from their source material (Wood, 1990; Bau, 1991; Haas et al., 1995). The earlier fluid generation of the HSB is aqueous and does not contain any significant amounts of CO_2, whereas the later fluid generations are aqueous-
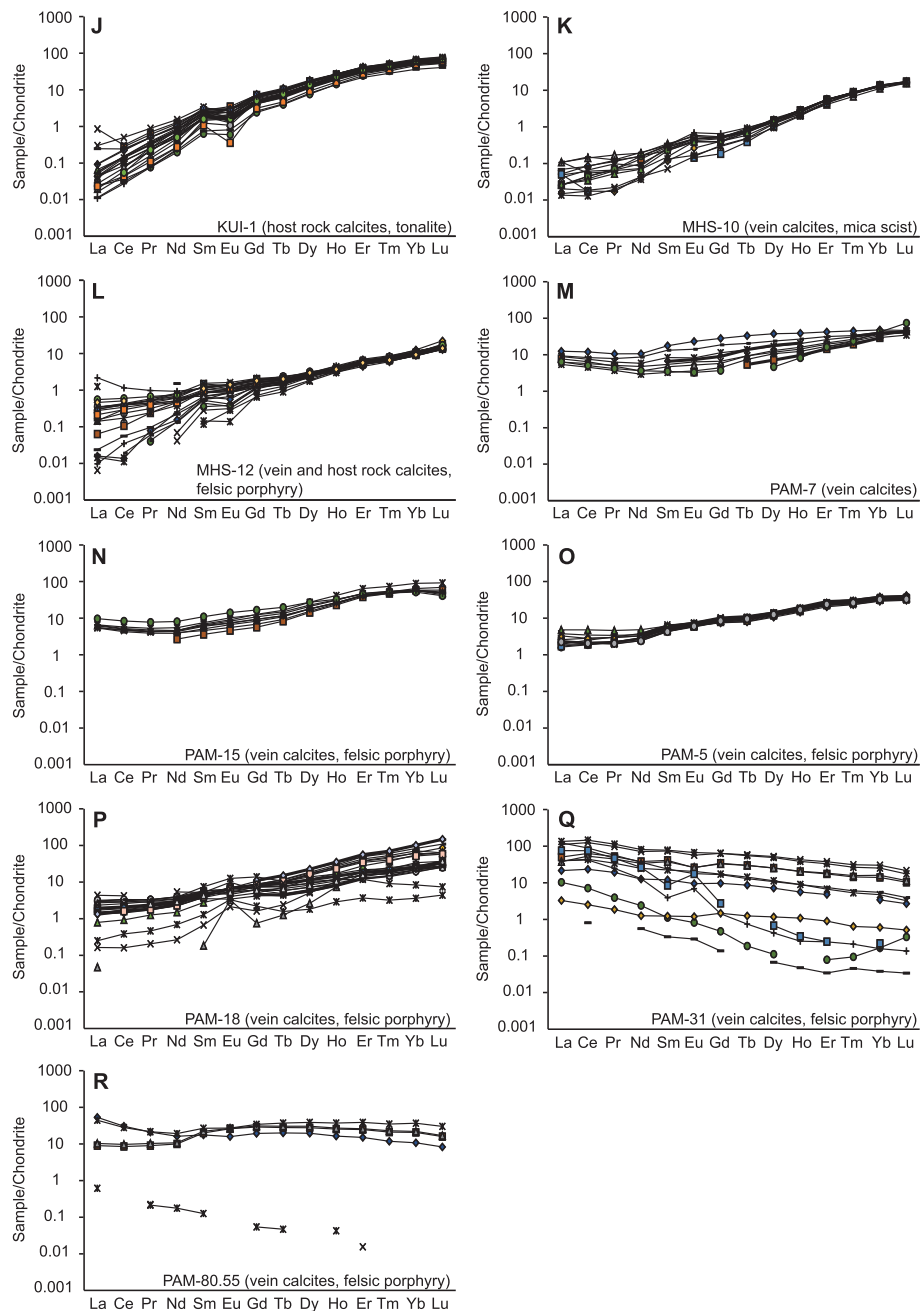
Fig. 12. (*continued*)

carbonic (Fusswinkel et al., 2017). While variations in the fractionation of REE in different calcite types of the HSB could potentially be explained by formation from successive fluid generations with different ligand chemistry, the REE patterns of clearly zoned calcite (PAM-80.55) do not always supports this. For example, the first generation of fluids which contain no CO_2 should produce calcites with cores that show LREE enrichment relative to the HREE. Instead, the more LREE enriched and fractionated patterns are observed in the outer zones of these calcites and the inner zones show less fractionated REE patterns (Fig. 14) which should be produced by fluids richer in CO_2.

Europium and cerium anomalies in hydrothermal calcites have been used for interpreting the ore-forming environments, particularly the oxidation state. Europium occurs mostly in the divalent state (Eu^{2+}) in hydrothermal and metamorphic fluids at temperatures above 250 °C and calcites formed in equilibrium with such fluids are typically characterized by positive Eu anomalies (e.g. Sverjensky, 1984; Bau and

Möller, 1992). Almost all hydrothermal calcites from the HSB show weak Eu anomalies, except few samples from the mafic and ultramafic metavolcanics which have pronounced positive Eu anomalies (samples PAM-51.0, PAM51.5 and PAE-9) and those from the Kuittila tonalite (KUI-1) which have weak negative Eu anomalies (Fig. 12; Table 5). By contrast, the whole-rock REE patterns of the mafic host rocks have generally weakly negative or positive Eu anomalies, if at all (O'Brien et al., 1993), and the data do not permit clear correlation of the Eu anomaly between hydrothermal calcites and host rocks. The komatiitic host rocks, on the other hand, shows positive Eu anomalies which could be correlated to the positive Eu anomaly seen in the calcites associated to the ultramafic host rocks (PAE-9). Similarly, the negative Eu anomalies in the Kuittila tonalite and associated calcites (KUI-1) can be correlated. The dependency of the calcite Eu anomalies on the respective anomalies in the host rocks is not clear, since only few samples, including the ultramafic rocks and tonalites show such a correlation.
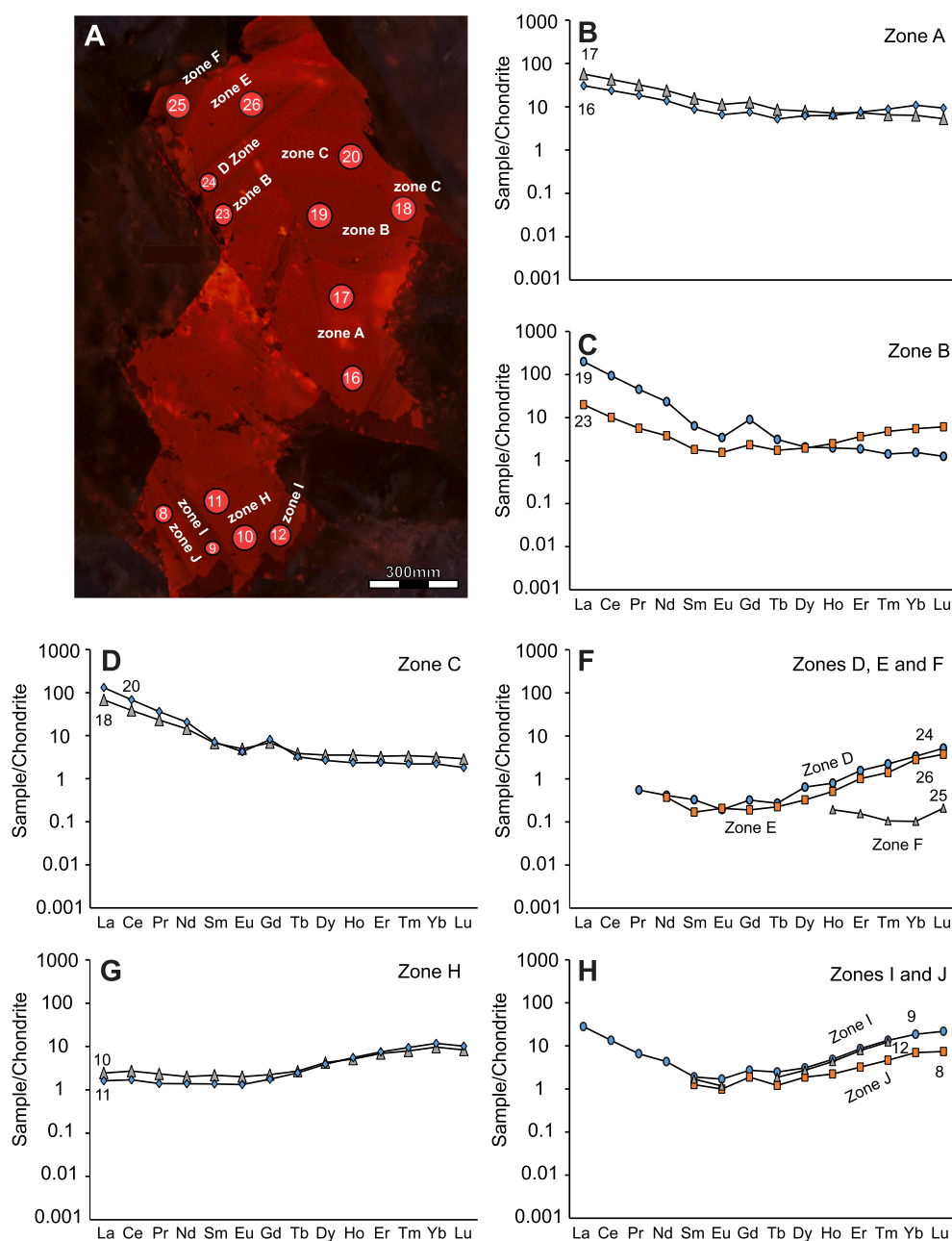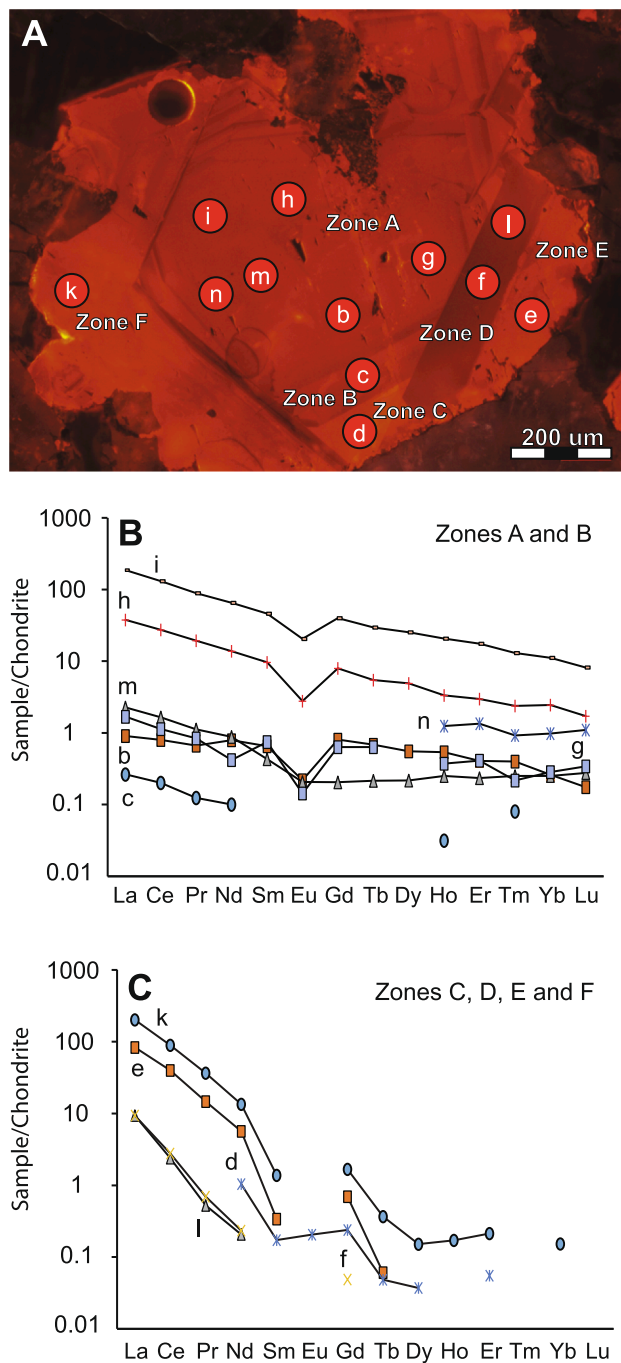
Fig. 13. Cathodoluminescence image and corresponding chondrite normalized REE patterns of complexly zoned hydrothermal calcites of sample PAM-7. (A) Cathodoluminescence image showing growth zoned calcite crystals. Red circles with lower case letter highlight the LA-ICP-MS spots analyzed and the upper-case letters label the different texturally distinguishable growth zones. (B-H) Chondrite normalized REE diagrams of individual calcite spot analyses of growth zones A to J.

Therefore, we suggest that variations in the magnitude of the Eu anomaly in the hydrothermal calcites are mainly a consequence of variations in the redox state of the hydrothermal fluid.

5.2. Significance of the Paleoproterozoic Svecofennian overprint

The younger Paleoproterozoic metamorphism related to the Svecofennian orogeny has been interpreted to have caused some locally occurring textural overprinting of minerals and the disturbance of certain isotope systematics. Therefore, the significance of the Svecofennian metamorphism for the hydrothermal carbonate chemistry of the HSB needs to be discussed. The evidence for Paleoproterozoic events is mainly based on K-Ar and Ar-Ar ages of micas and poorly constrained Rb-Sr ages of tourmalines (O'Brien et al., 1993; Molnár

et al., 2016b). The Pb isotope data of the sulfide minerals in the HSB gold deposits are somewhat controversial. Vaasjoki et al. (1993) found no evidence of the Paleoproterozoic metamorphic overprint in the Pb isotope systematics of the Archean galenas, while Molnár et al. (2016b) explained the somewhat variable Pb isotope data of galenas analyzed by LA-MC-ICP-MS by mixing of less radiogenic lead of the Archean ores with more radiogenic lead from the host rocks during the Paleoproterozoic event. On the other hand, the preserved sulfur isotope disequilibrium of sulfide minerals indicates that the Paleoproterozoic event has insignificant effect to the overall Archean sulfur isotope signatures (Molnár et al., 2016a). The stable isotope signatures of hydrothermal carbonates from the gold deposits of the HSB have been mainly interpreted in terms of the Archean ore formation. The carbon isotope studies of carbonates show uniform values of $\delta^{13}C_{PDB}$ ranging from

Fig. 14. Cathodoluminescence image and corresponding chondrite normalized REE patterns of complexly zoned hydrothermal calcites of sample PAM-80.55. Red circles with lower case letter highlight the LA-ICP-MS spots analyzed and the upper-case letters label the different texturally distinguishable growth zones. (B-H) Chondrite normalized REE diagrams of individual calcite spot analyses of growth zones A to F.

-8.6 to $-10‰$, while the $\delta^{18}O_{SMOW}$ values show a larger variation, from 4.7 to 18.8‰, which is comparable to the range shown by hydrothermal quartz from the HSB deposits (Karhu et al., 1993). The preserved and uniform $\delta^{13}C_{PDB}$ values have been interpreted as being representative for the Archean gold mineralizing fluids (although somewhat lower compared to other Archean gold deposits worldwide) showing only small differences in composition between individual deposits. The interpretation of the large range in $\delta^{18}O_{SMOW}$ in the hydrothermal calcites and quartz in the HSB deposits is less clear. Alternative explanations are hydrothermal alteration related to fluids
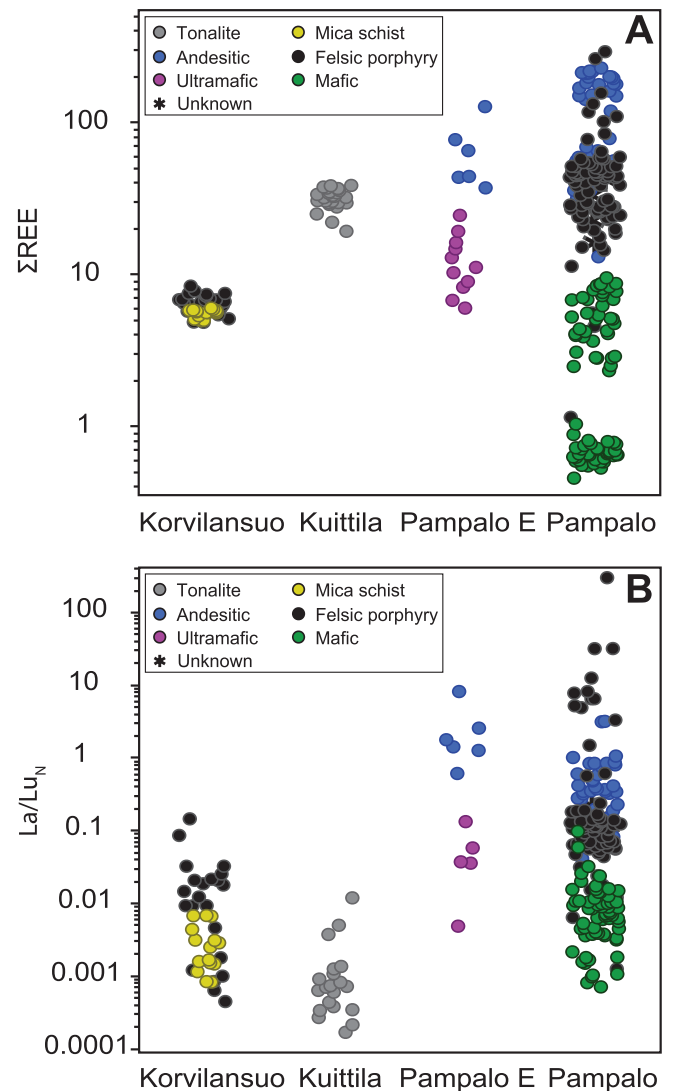

Fig. 15. Summary plots of (A) total REE concentrations (ΣREE) and (B) the normalized La/Lu ratio (La/Lu$_N$) of different calcites from the HSB, classified according to locality and host rock lithology.

derived from cooling of the Archean granitoids, or local reaction of the Archean gold mineralization with hydrothermal waters circulating during the Paleoproterozoic metamorphism (O'Brien et al., 1993; Karhu et al., 1993).

There are several arguments which, taken together, demonstrate that the principal calcite formation in the hydrothermal gold deposits occurred during the Archean mineralization event and has essentially not been affected by the Paleoproterozoic event: (1) hydrothermal calcites are typically observed in the ore veins and hydrothermal alteration zones of the Archean gold deposits in the HSB (Kojonen et al., 1993; Karhu et al., 1993; this study); (2) some calcite bearing hydrothermal veins which are possibly associated to the Paleoproterozoic event are inferred but they occur very locally (Molnár et al. 2016b; Sorjonen-Ward, personal communication); (3) mass balance analysis of hydrothermal alteration in the HSB deposits has demonstrated that enrichment in CO_2 (as well as of Mo and W) can be clearly correlated with Au grades and linked to the Archean ore assemblages (Bornhorst and Rasilainen, 1993); (4) the gold bearing ore assemblages in veins and altered wall rocks show virtually no evidence of remobilization by later events except very locally (Kojonen et al., 1993; Molnár et al. 2016b); (5) no significant gold occurrences and/or hydrothermal alteration has been identified in relation to late brittle or brittle-ductile
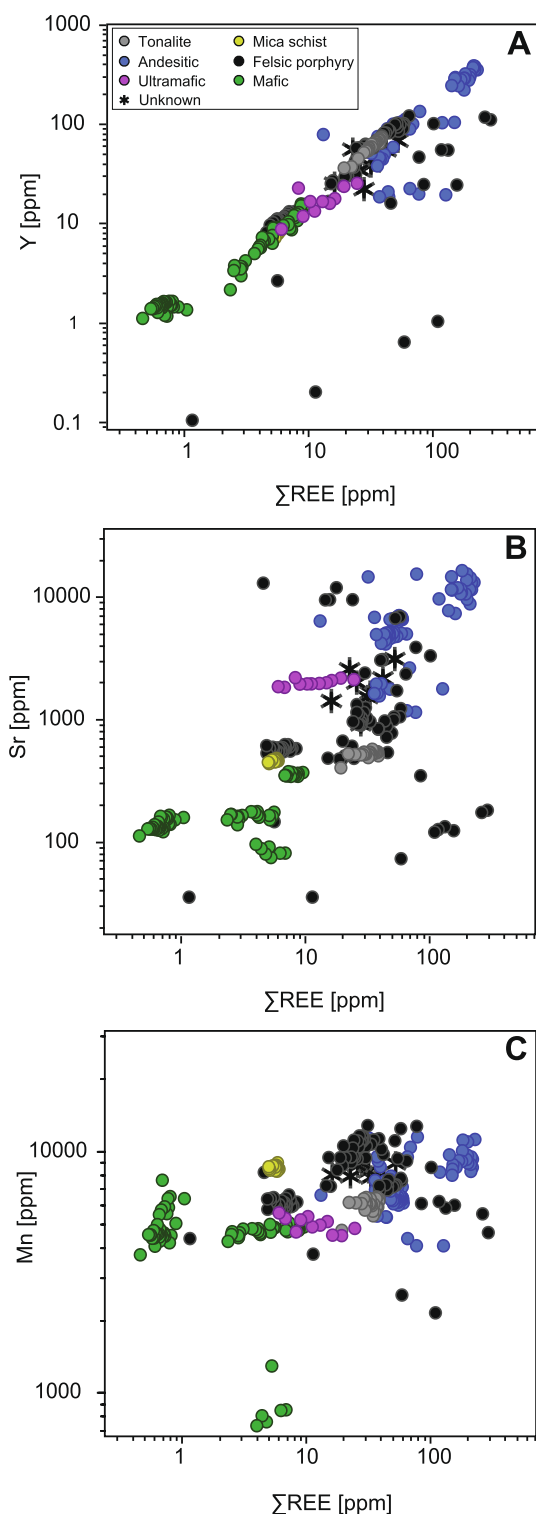
Fig. 16. Variation diagrams showing (A) Y concentration, (B) Sr concentration, and (C) Mn concentration as a function of the total REE concentration (ΣREE) for different calcites from the HSB.

structures of the HSB (Sorjonen-Ward 1993); (6) the carbon isotope data of carbonate minerals in HSB show mainly Archean signatures (Karhu et al., 1993). Some minor textural and geochemical features of the calcites, such as the presence of late chemically distinct growth zones and overgrowth of rims on otherwise unzoned crystals, may reflect the chemically evolving Archean fluid system or the later Paleoproterozoic event. Because these calcite types occur only as small

texturally distinct zones and very locally and are volumetrically insignificant, their presence does not affect the interpretation of the bulk of the calcite data in terms of the Archean gold mineralizing hydrothermal system.

6. Conclusions

1) The hydrothermal calcites from the HSB, including vein hosted and disseminated calcite from the ultramafic, mafic and andesitic metavolcanics rocks, metasedimentary rocks, felsic porphyry dikes and tonalites show very low concentrations of most trace elements, with the notable exception of Sr, Y, Mg, Fe and Mn.

2) Some hydrothermal calcite crystals show a clear growth zoning in CL images, and successive growth zones show clear differences in their trace element concentrations and their REE patterns. These textural and chemical variations are best explained by multi-stage calcite growth from a chemically evolving fluid or successive fluid generations with different composition.

3) When comparing the data for the Korvilansuo and Pampalo gold deposits, the Sr, Y and Mn concentrations in calcite show a positive correlation with the total REE content (ΣREE) as well as distinct differences between host rock types. This demonstrates that fluid-rock interaction with local host rocks has affected the trace element composition of hydrothermal calcites.

4) The majority of the shale normalized REE patterns of the calcites show preferential HREE enrichment over LREE, and the REE patterns of the calcites are different from those of their respective bulk host rocks. This shows that the REE patterns of the calcites are not controlled by local fluid-rock interaction but rather inherited from the hydrothermal fluids. The REE patterns are compatible with an ultimately metamorphic source and not compatible with a magmatic-hydrothermal origin.

Acknowledgements

Appendix A. Supplementary data

Supplementary data to this article can be found online at https://doi.org/10.1016/j.oregeorev.2019.103006.

References

Barker, S.L.L., Cox, S.F., Eggins, S.M., Gagan, M.K., 2006. Microchemical evidence for episodic growth of antitaxial veins during fracture-controlled fluid flow. Earth Planet. Sc. Lett. 250, 331–344.

Barker, S.L.L., Cox, S.F., 2011. Oscillatory zoning and trace element incorporation in hydrothermal minerals: insights from calcite growth experiments. Geofluids 11, 45–56.

Bau, M., 1991. Rare-earth element mobility during hydrothermal and metamorphic fluid-rock interaction and the significance of the oxidation state of europium. Chem. Geol. 93, 219–230.

Bau, M., 1993. Rare-earth element mobility during hydrothermal and metamorphic fluid-rock interaction and the significance of the oxidation state of europium. Chem. Geol. 93, 219–230.

Bau, M., Möller, P., 1992. Rare earth element fractionation in metamorphogenic hydrothermal calcite, magnesite and siderite. Miner. Petrol. 45, 231–245.

Bornhorst, T.J., Rasilainen, K., Nurmi, P.A., 1993. In: Geochemical Character of Lithologic Units in the Late Archean Hattu Schist Belt, Ilomantsi, Eastern Finland. Geological Survey of Finland Special Paper 17, pp. 133–145.

Bornhorst, T.J., Rasilainen, K., 1993. In: Mass Transfer During Hydrothermal Alteration Associated with Au Mineralization within the Late Archean Hattu Schist Belt, Ilomantsi, Eastern Finland. Geological Survey of Finland Special Paper 17, pp.

273–289.

Boynton, W.V., 1984. Cosmochemistry of the rare earth elements: meteorite studies. In: Henderson, P. (Ed.), Rare Earth Element Geochemistry. Elsevier, Amsterdam, pp. 63–114.

Budd, D.A., Hammes, U., Ward, W.B., 2000. Cathodoluminescence in calcite cements: new insights on Pb and Zn sensitizing, Mn activations, and Fe quenching at low trace-element concentrations. J. Sediment. Res. 70, 217–226.

Dubinina, E.O., Chugaev, A.V., Ikonnikova, T.A., Adveenko, A.S., Yakushev, A.I., 2014. Sources and fluid regime of quartz-carbonate veins at the Sukhoi Log gold deposit, Baikal-Patom Highland. Petrology 22, 329–358.

Fairchild, I.J., 1983. Chemical controls of cathodoluminescence of natural dolomites and calcites: new data and review. Sedimentology 30, 579–583.

Frimmel, H.E., 2008. Earth's continental crustal gold endowment. Earth Planet. Sc. Lett. 267, 45–55.

Fusswinkel, T., Wagner, T., Wenzel, T., Wälle, M., Lorenz, J., 2013. Evolution of un-conformity-related Mn-Fe-As vein mineralization, Sailauf (Germany): insight from major and trace elements in oxide and carbonate minerals. Ore. Geol. Rev. 50, 28–51.

Fusswinkel, T., Wagner, T., Sakellaris, G., 2017. Fluid evolution of the Neoarchean Pampalo orogenic gold deposit (E Finland): constraints from LA-ICPMS fluid inclusion microanalysis. Chem. Geol. 450, 96–121.

Gabitov, R.I., Sadekov, A., Leinweber, A., 2014. Crystal growth rate effect on Mg/Ca and Sr/Ca distribution between calcite and fluid: an in-situ approach. Chem. Geol. 367, 70–82.

Gebre-Mariam, M., Hagemann, S.G., Groves, D.J., 1995. A classification scheme for epigenetic Archaean lode-gold deposits. Miner. Deposita 30, 408–410.

Goldfarb, R.J., Baker, T., Dubé, B., Groves, D.I., Hart, C.J.R., Gosselin, P., 2005. Distribution, character, and genesis of gold deposits in metamorphic terranes. Econ. Geol. 100th Anniversary Volume, 407–450.

Goldfarb, R.J., Groves, D.I., 2015. Orogenic gold: common or evolving fluid and metal sources through time. Lithos 233, 2–26.

Goldfarb, R.J., Groves, D.I., Gardoll, S., 2001. Orogenic gold and geologic time; a global synthesis. Ore Geol. Rev. 18, 1–75.

Groves, D.I., Goldfarb, R.J., Gebre-Mariam, M., Hagemann, S.G., Robert, F., 1998. Orogenic gold deposits – a proposed classification in the context of their crustal distribution and relationship to other gold deposit types. Ore Geol. Rev. 13, 7–27.

Groves, D.I., Goldfarb, R.J., Robert, F., Hart, C.J.R., 2003. Gold deposits in metamorphic belts: overview of current understanding, outstanding problems, future research, and exploration significance. Econ. Geol. 98, 1–29.

Guillong, M., Meier, D.L., Allan, M.M., Heinrich, C.A., Yardley, B.W.D., 2008. SILLS: a MATLAB-based program for the reduction of laser ablation ICP-MS data of homogeneous materials and inclusions. Mineralogical Association of Canada Short Course Series 40, 328–333.

Haas, J.R., Shock, E.L., Sassani, D.C., 1995. Rare-earth elements in hydrothermal systems – estimates of standard partial molal thermodynamic properties of aqueous complexes of the rare-earth elements at high-pressures and temperatures. Geochim. Cosmochim. Ac. 59, 4329–4350.

Hazarika, P., Mishra, B., Pruseth, K.L., 2015. Diverse tourmaline compositions from orogenic gold deposits in the Hutti-Maski greenstone belt, India: implications for sources of ore-forming fluids. Econ. Geol. 110, 337–353.

Hazarika, P., Mishra, B., Pruseth, K.L., 2016. Scheelite, apatite, calcite and tourmaline compositions from the late Archean Hutti orogenic gold deposit: implications for analogous two stage ore fluids. Ore Geol. Rev. 72, 989–1003.

Heilimo, E., Halla, J., Huhma, H., 2011. Single-grain zircon U-Pb age constraints of the western and eastern sanukitoid zones in the Finnish part of the Karelian Province. Lithos 121, 87–99.

Heinrich, C.A., Pettke, T., Halter, W.E., Aigner-Torres, M., Audetat, A., Günther, D., Hattendorf, B., Bleiner, D., Guillong, M., Horn, I., 2003. Quantitative multi-element analysis of minerals, fluid and melt inclusions by laser-ablation inductively-coupled plasma mass-spectrometry. Geochim. Cosmochim. Ac. 67, 3473–3497.

Hölttä, P., Heilimo, E., Huhma, H., Kontinen, A., Mertanen, S., Mikkola, P., Paavola, J., Peltonen, P., Semprich, J., Slabunov, A., Sorjonen-Ward, P., 2012. In: The Archaean of the Karelia Province in Finland. Geological Survey of Finland Special Paper 54, pp. 21–73.

Hölttä, P., Lehtonen, E., Lahaye, Y., Sorjonen-Ward, P., 2016. Metamorphic evolution of the Ilomantsi greenstone belt in the Archean Karelia Province, eastern Finland. Geol. Soc. Spec. Publ. 449, 231–250.

Huhma, H., Mänttäri, I., Peltonen, P., Kontinen, A., Halkoaho, T., Hanski, E., Hokkanen, T., Hölttä, P., Juopperi, H., Konnunaho, J., Layahe, Y., Luukkonen, E., Pietikäinen, K., Pulkkinen, A., Sorjonen-Ward, P., Vaasjoki, M., Whitehouse, M., 2012. In: The Age of the Archaean Greenstone Belts in Finland. Geological Survey of Finland Special Paper 54, pp. 74–175.

Kalliomäki, H., Wagner, T., Fusswinkel, T., Sakellaris, G., 2017. Major and trace element geochemistry of tourmalines from Archean orogenic gold deposits: proxies for the origin of gold mineralizing fluids? Ore Geol. Rev. 91, 906–927.

Käpyaho, A., Molnár, F., Sorjonen-Ward, P., Mänttäri, I., Sakellaris, G., Whitehouse, M.J., 2017. New U-Pb age constrains for the timing of gold mineralization at the Pampalo gold deposit, Archean Hattu schist belt, eastern Finland, obtained from hydrothermally altered and recrystallized zircon. Precambrian Res. 289, 48–61.

Karhu, J.A., Nurmi, P.A., O'Brien, H.E., 1993. In: Carbon and Oxygen Isotope Ratios of Hydrothermal Carbonates Associated with Gold Mineralization in the Late Archean Hattus Schist Belt, Ilomantsi, Eastern Finland. Geological Survey of Finland Special 17, pp. 307–316.

Kojonen, K., Johanson, B., O'Brien, H.E., Pakkanen, L., 1993. In: Mineralogy of Gold Occurrences in the late Archean Hattu Schist belt, Ilomantsi, Eastern Finland. Geological Survey of Finland Special Paper 17, pp. 233–271.

Kontak, D.J., Jackson, S.J., 1995. Laser-Ablation ICP-MS micro-analysis of calcite cement

from a Mississippi Valley-type Zn-Pb deposit, Nova Scotia: dramatic variability in REE content on macro and micro scale. Can. Mineral. 33, 445–467.

Kontak, D.J., Jackson, S.J., 1999. Documentation of variable trace- and rare-earth-element abundances in carbonates from auriferous quartz veins in Meguma lode-gold deposit, Nova Scotia. Can. Mineral. 37, 469–488.

Kontinen, A., Paavola, J., Lukkarinen, H., 1992. K-Ar ages of hornblende and biotite from the late Archean rock of eastern Finland-interpretation and discussion of tectonic implications. Geol. Surv. Finl. Bull. 365, 1–31.

Krienitz, M.S., Trumbull, R.B., Hellmann, A., Kolb, J., Meyer, F.M., Wiedenbeck, M., 2008. Hydrothermal gold mineralization at the Hira-Buddini gold mine, India: constraints on fluid evolution and fluid sources from boron isotopic compositions of tourmaline. Miner. Deposita 43, 421–434.

Lahann, R.W., Siebert, R.M., 1982. A kinetic model for distribution coefficients and application to Mg-calcites. Geochim. Cosmochim. Ac. 46, 2229–2237.

Lorens, R.B., 1981. Sr, Cd, Mn and Co distribution coefficients in calcite as a function of calcite precipitation rate. Geochim. Cosmochim. Ac. 45, 553–561.

McIntire, W.L., 1963. Trace element partition coefficients – a review of theory and applications to geology. Geochim. Cosmochim. Ac. 27, 1209–1264.

Mikucki, E.J., 1998. Hydrothermal transport and depositional processes in Archean lode-gold systems: a review. Ore Geol. Rev. 13, 307–321.

Möller, P., Morteani, G., Hoefs, J., Parekh, P.P., 1979. The origin of the ore-bearing solution in the Ob-Zn vein of the western Harz, Germany, as deduced from rare earth element and isotope distributions in calcite. Chem. Geol. 26, 197–215.

Möller, P., Morteani, G., Dulski, P., 1984. The origin of the calcites from Pb-Zn veins in the Harz mountains, Federal Republic of Germany. Chem. Geol. 45, 91–112.

Möller, P., Lüders, V., Schröder, J., Luck, J., 1991. Element partitioning in calcite as a function of solution flow rate: a study on vein calcites from the Harz Mountains. Miner. Deposita 26, 175–179.

Molnár, F., Mänttäri, I., O'Brien, H., Lahaye, Y., Johanson, B., Käpyaho, A., Sorjonen-Ward, P., Whitehouse, M., Sakellaris, G., 2016a. Boron, sulphur and copper isotope systematics in the orogenic gold deposits of the Archaean Hattu schist belt, eastern Finland. Ore Geol. Rev. 77, 133–162.

Molnár, F., O'Brien, H., Lahaye, Y., Käpyaho, A., Sorjonen-Ward, P., Hyodo, H., Sakellaris, G., 2016b. Signatures of multiple mineralization processes in the Archean orogenic gold deposit of the Pampalo mine, Hattu schist belt, eastern Finland. Econ. Geol. 111, 1659–1703.

Mucci, A., Morse, J.W., 1983. The incorporation of Mg^{2+} and Sr^{2+} into calcite overgrowths: influences of growth rate and solution composition. Geochim. Cosmochim. Ac. 47, 217–233.

Nurmi, P.A., Sorjonen-Ward, P., Damstén, M., 1993. In: Geological Setting, Characteristics and Exploration History of Mesothermal Gold Occurrences in the Late Archean Hattu Schist Belt, Ilomantsi, Eastern Finland. Geological Survey of Finland Special Paper 17, pp. 193–231.

O'Brien, H., Nurmi, P.A., Karhu, J.A., 1993. In: Oxygen, Hydrogen and Strontium Isotopic Composition of Gold Mineralizations in the Late Archean Hattu Schist Belt, Ilomantsi, Eastern Finland. Geological Survey of Finland Special Paper 17, pp. 291–306.

Paquette, J., Reeder, R.J., 1990. New type of compositional zoning in calcite: insights into crystal-growth mechanisms. Geology 18, 1244–1247.

Paquette, J., Reeder, R.J., 1995. Relationship between surface structure, growth mechanism, and trace element incorporation in calcite. Geochim. Cosmochim. Ac. 59, 735–749.

Parkkinen, J., 1994. In: The Ward Gold Deposit, Ilomantsi; Mineral Resource Estimate. Geological Survey of Finland Report M19/4333/94/2/10, pp. 105.

Perry, E.P., Gysi, A.P., 2018. Rare earth elements in mineral deposits: speciation in hydrothermal fluids and partitioning in calcite. Geofluids. https://doi.org/10.1155/2018/5382480.

Pettke, T., Diamond, L.W., Kramers, J.D., 2000. Mesothermal gold lodes in the northwestern Alps: a review of genetic constraints from radiogenic isotopes. Eur. J. Mineral. 12, 213–230.

Phillips, G.N., Powell, R., 2010. Formation of gold deposits: a metamorphic devolatilization model. J. Metamorph. Geol. 28, 689–718.

Poutiainen, M., Partamies, S., 2003. Fluid inclusion characteristics of auriferous quartz veins in Archean and Paleoproterozoic greenstone belts of eastern and southern Finland. Econ. Geol. 98, 1355–1369.

Reeder, R.J., 1996. Interaction of divalent cobalt, zinc, cadmium, and barium with the calcite surface during layer growth. Geochim. Cosmochim. Ac. 60, 1543–1552.

Reeder, R.J., Grams, J.C., 1987. Sector zoning in calcite cement crystals: implications for trace element distributions in carbonates. Geochim. Cosmochim. Ac. 51, 187–194.

Ridley, J.R., Diamond, L.W., 2000. Fluid chemistry of orogenic lode gold deposits and implications for genetic models. Rev. Econ. Geol. 13, 141–162.

Rimstidt, J.D., Balog, A., Webb, J., 1998. Distribution of trace elements between carbonate minerals and aqueous solutions. Geochim. Cosmochim. Ac. 62, 1851–1863.

Sarangi, S., Srinivasan, R., Balaram, V., 2013. REE geochemistry of auriferous quartz carbonate veins of Neoarchean Ajjanahalli gold deposit, Chitradurga schist belt, Dharwar Craton. India. Geosci. Front. 4, 231–239.

Sorjonen-Ward, P., 1993. In: An Overview of Structural Evolution and Lithic Units Within and Intruding the Late Archean Hattu Schist Belt, Ilomantsi, Eastern Finland. Geological Survey of Finland Special Paper 17, pp. 9–102.

Sorjonen-Ward, P., Claoué-Long, J., 1993. In: Preliminary Note on Ion Probe Results for Zircons from the Silvevaara Granodiorite, Ilomantsi, Eastern Finland. Geological Survey of Finland Special Paper 18, pp. 25–29.

Sorjonen-Ward, P., Luukkonen, E.J., 2005. Archean rocks. In: Lehtinen, M., Nurmi, P.A., Rämö, O.T. (Eds.), Precambrian Geology of Finland. Elsevier, pp. 19–99.

Sorjonen-Ward, P., Hartikainen, A., Nurmi, P.A., Rasilainen, K., Schaubs, P., Zhang, Y., Liikanen, J., 2015. Exploration targeting and geological context of gold mineralization in the Neoarchean Ilomantsi greenstone belt in eastern Finland. In: Maier, W.D.,

Lahtinen, R., O'Brien, H. (Eds.), Mineral Deposits of Finland. Elsevier, pp. 435–466.

Sverjensky, D.A., 1984. Europium redox equilibria in aqueous solution. Earth Planet. Sc. Lett. 67, 70–78.

Terakado, Y., Masuda, A., 1988. The coprecipitation of rare-earth elements with calcite and aragonite. Chem. Geol. 69, 103–110.

Tesoriero, A.J., Pankow, J.F., 1996. Solid solution distribution of Sr^{2+}, Ba^{2+}, and Cd^{2+} to calcite. Geochim. Cosmochim. Ac. 60, 1053–1063.

Vaasjoki, M., Sorjonen-Ward, P., Lavikainen, S., 1993. In: U-Pb age Determinations and Sulfide Pb-Pb Characteristics from the Late Archean Hattu Schist Belt, Ilomantsi, Eastern Finland. Geological Survey of Finland Special Paper 17, pp. 103–131.

Veizer, J., 1983. Trace elements and isotopes in sedimentary carbonates. Rev. Mineral. 11, 265–299.

Voigt, M., Mavromatis, V., Oelkers, E.H., 2017. The experimental determination of REE partition coefficient in the water-calcite system. Chem. Geol. 462, 30–43.

Wang, L.G., McNaughton, N.J., Groves, D.I., 1993. An overview of the relationship between granitoid intrusions and gold mineralisation in the Archaean Murchison Province. Western Australia. Miner. Deposita 28, 482–494.

Wogelius, R.A., Fraser, D.G., Wall, G.R.T., Grime, G.F., 1997. Trace element and isotopic zonation in vein calcite from the Mendip Hills, UK, with spatial-process correlation analysis. Geochim. Cosmochim. Ac. 61, 2037–2051.

Wood, S., 1990. The aqueous geochemistry of the rare-earth elements and yttrium: 2. Theoretical predictions of speciation in hydrothermal solutions to 350 °C at saturation water-vapor pressure. Chem. Geol. 88, 99–125.

Yardley, B.W.D., Cleverley, J.S., 2013. The role of metamorphic fluids in the formation of ore deposits. Geol. Soc. Spec. Publ. 393, 117–134.

Zhong, A., Mucci, A., 1995. Partitioning of rare earth elements (REEs) between calcite and seawater solutions at 25°C and 1 atm, and high dissolved REE concentrations. Geochim. Cosmochim. Ac. 59, 443–453.

Zoheir, B., Moritz, R., 2014. Fluid evolution in the El-Sid gold deposit, Eastern Desert. Egypt. Geol. Soc. Spec. Publ. 402, 147–175.